Vectorial and random effects in self-focusing and in multiple filamentation

Gadi Fibich*, Boaz Ilan

Department of Applied Mathematics, Tel Aviv University, Tel Aviv 69978, Israel

Abstract

The standard explanation for multiple filamentation of laser beams is that breakup of cylindrical symmetry is initiated by noise in the input beam. In this study we propose an alternative deterministic explanation based on vectorial effects. We derive a scalar equation from the vector Helmholtz equation that describes self-focusing in the presence of vectorial and nonparaxial effects. Numerical simulations of the scalar equation show that when the input beam is sufficiently powerful, vectorial effects lead to multiple filamentation. We compare multiple filamentation due to vectorial effects with the one due to noise, and suggest how to decide which of the two leads to multiple filamentation in experiments. We also show that vectorial effects and nonparaxiality have the same effect on self-focusing of a single filament, leading to the arrest of catastrophic collapse, followed by focusing–defocusing oscillations. The magnitude of vectorial effects is, however, significantly larger than that of nonparaxiality. © 2001 Elsevier Science B.V. All rights reserved.

1. Introduction

The nonlinear Schrödinger equation (NLS) is the model equation for the propagation of intense laser beams in a Kerr medium. Based on the NLS equation, Kelley [26] predicted in 1965 that intense laser beams whose input power is above a certain threshold would undergo "catastrophic" self-focusing in a finite propagation distance. Although this prediction was confirmed experimentally, the NLS, as a physical model for self-focusing, has several weaknesses:

1. According to the NLS model, the beam intensity becomes infinite at a finite distance. As a result, the NLS model fails to describe beam propagation beyond that point.

---

* Corresponding author. Tel.: +972-3-640-7164; fax: +972-3-640-9357.
E-mail address: fibich@post.tau.ac.il (G. Fibich).

2. The NLS is the leading order approximation to Maxwell's equations. However, because the NLS is extremely sensitive to the addition of small terms [20], one cannot ignore the remaining terms simply because they appear to be small.
3. According to the NLS model, beams with cylindrically symmetric input profile should remain cylindrically symmetric during propagation. However, self-focusing experiments in solids, liquids, and gases have shown that catastrophic self-focusing is often preceded by *multiple filamentation*, [1] in which a single input beam breaks-up into several long and narrow filaments [1,3,7,8,10–12,14,15,28,30,36–38]. Therefore, a self-focusing model should include a mechanism that breaks-up the cylindrical symmetry and leads to multiple filamentation.

In this study we focus on the role of vectorial effects in self-focusing. As we shall see, these effects, which are neglected in the derivation of the NLS model from Maxwell's equations, relate to all of the above weaknesses of the NLS model:

1. Vectorial effects arrest the blowup. As a result, the NLS model with vectorial effects can be used to describe beam propagation beyond the NLS blowup point.
2. Vectorial effects, although small in magnitude, have a large effect on beam propagation. In fact, we show that vectorial effects have a larger effect than nonparaxiality.
3. For over 30 years, the standard explanation for multiple filamentation, due to Bespalov and Talanov [4], has been that it is initiated by *random* noise in the input-beam profile. In this study we show that the *deterministic* vectorial effects can also lead to multiple filamentation.

The paper is organized as follows: In Section 2 we present the vector Helmholtz model, which leads to the NLS. In Section 2.2 we give a short review of NLS theory. In Section 3 we approximate the vector Helmholtz equation with a scalar PDE, which describes self-focusing in the presence of vectorial and nonparaxial effects. In Section 4 we present numerical simulations that show that vectorial effects can lead to multiple filamentation. In Section 5 we use modulation theory to reduce the scalar PDE to an ODE for self-focusing dynamics of a single filament in the presence of vectorial and nonparaxial effects. In Section 6 we discuss the possibility that noise in the input beam leads to multiple filamentation. In Section 7 we compare the noise and the vectorial effects explanations for multiple filamentation. In Section 8 we suggest a simple experiment for deciding whether multiple filamentation is due to vectorial effects or not. In Section 9 we describe the numerical methods used in our simulations, and show that reflections from the numerical boundary can lead to "artificial" filaments.

2. The vectorial model

The propagation of an intense cw laser beam in a Kerr medium is described by the *vector Helmholtz equations* [6,13]

$$\Delta \vec{\mathcal{E}}(x, y, z) - \nabla(\nabla \cdot \vec{\mathcal{E}}) + k_0^2 \vec{\mathcal{E}} = -\frac{k_0^2}{\epsilon_0 n_0^2} \vec{\mathcal{P}}_{NL}, \tag{1}$$

$$\nabla \cdot \vec{\mathcal{E}} = -\frac{1}{\epsilon_0 n_0^2} \nabla \cdot \vec{\mathcal{P}}_{NL}, \tag{2}$$

where $\Delta = \partial_{xx} + \partial_{yy} + \partial_{zz}$, $\vec{\mathcal{E}} = (\mathcal{E}_1, \mathcal{E}_2, \mathcal{E}_3)$ is the electric field, $\vec{\mathcal{P}}_{NL}$ the nonlinear polarization vector, ϵ_0 the vacuum permittivity, n_0 the medium's linear index of refraction, and k_0 the wavenumber. When the Kerr medium

---

[1] Multiple filamentation is also called multiple-foci, small-scale filaments, or beam-breakup.

Table 1
Values of γ [6] and $C_{\text{vec}}(\gamma)$ [in Eq. (31)] for common Kerr mechanisms

Kerr mechanism	γ	$C_{\text{vec}}(\gamma)$
Electrostriction	0	5.7
Nonresonant electrons	0.5	7.6
Molecular orientation	3	9.8

is isotropic and homogeneous, the nonlinear polarization vector is given by [31,32]

$$\vec{\mathcal{P}}_{\text{NL}}(\vec{\mathcal{E}}) = \frac{4\epsilon_0 n_0 \bar{n}_2}{1+\gamma}[(\vec{\mathcal{E}} \cdot \vec{\mathcal{E}}^*)\vec{\mathcal{E}} + \gamma(\vec{\mathcal{E}} \cdot \vec{\mathcal{E}})\vec{\mathcal{E}}^*], \tag{3}$$

where $\vec{\mathcal{E}}^*$ is the complex-conjugate of $\vec{\mathcal{E}}$, $\bar{n}_2$ the Kerr coefficient,[2] and γ a constant, whose value depends on the physical origin of the Kerr effect (see Table 1). It is instructive to rewrite relation (3) as

$$\vec{P}_{\text{NL}}(\vec{\mathcal{E}}) = \frac{4\epsilon_0 n_0 \bar{n}_2}{1+\gamma} \left[|\vec{\mathcal{E}}|^2 \begin{pmatrix} 1 & 0 & 0 \\ 0 & 1 & 0 \\ 0 & 0 & 1 \end{pmatrix} + \gamma \begin{pmatrix} |\mathcal{E}_1|^2 & \mathcal{E}_2\mathcal{E}_1^* & \mathcal{E}_3\mathcal{E}_1^* \\ \mathcal{E}_1\mathcal{E}_2^* & |\mathcal{E}_2|^2 & \mathcal{E}_3\mathcal{E}_2^* \\ \mathcal{E}_1\mathcal{E}_3^* & \mathcal{E}_2\mathcal{E}_3^* & |\mathcal{E}_3|^2 \end{pmatrix} \right] \begin{pmatrix} \mathcal{E}_1 \\ \mathcal{E}_2 \\ \mathcal{E}_3 \end{pmatrix}.$$

When $\gamma = 0$ the Kerr effect is only "semi-vectorial", in the sense that $\vec{P}_{\text{NL}} = 4\epsilon_0 n_0 \bar{n}_2 |\vec{\mathcal{E}}|^2 \vec{\mathcal{E}}$. In other words, the semi-vectorial Kerr effect is given by the scalar index of refraction

$$n^2 = n_0^2 + 4n_0\bar{n}_2|\vec{\mathcal{E}}|^2. \tag{4}$$

However, when $\gamma \neq 0$, the Kerr effect is genuinely vectorial, i.e., it cannot be written in the form (4).

2.1. From vector Helmholtz to NLS

Because of the linear and nonlinear coupling between the components of $\vec{\mathcal{E}}$, direct analysis or simulations of the system (1)–(3) is hard. Therefore, it is customary to approximate the vector Helmholtz equation with the NLS, which is much more amenable to analysis and simulations. We now outline the derivation of the NLS from the vector Helmholtz equation. A detailed derivation is given in Section 3.1.

We set the coordinate system so that the Kerr medium is located at $z \geq 0$, the input laser beam is linearly polarized in the x direction, and the beam propagates in the positive z direction as it enters the Kerr medium at $z = 0$. Because the input beam is linearly polarized, it is usually assumed that the beam remains linearly polarized as it propagates inside the Kerr medium, i.e., that $\mathcal{E}_2 \equiv \mathcal{E}_3 \equiv 0$ for $z \geq 0$. In that case, the Kerr effect (3) is given by the scalar relation $n^2 = n_0^2 + 4n_0\bar{n}_2|\mathcal{E}_1|^2$. If one further uses the approximation $\nabla \cdot \vec{\mathcal{E}} = 0$, then, to leading order, the vector Helmholtz equations reduce to the scalar nonlinear Helmholtz equation for $\mathcal{E}_1$:

$$\Delta\mathcal{E}_1(x, y, z) + k^2\mathcal{E}_1 = 0, \quad k^2 = k_0^2\left(1 + \frac{4\bar{n}_2}{n_0}|\mathcal{E}_1|^2\right). \tag{5}$$

Separating the fast oscillations from the slowly varying amplitude, i.e., $\mathcal{E}_1 = \mathcal{A}_1(x, y, z)\,e^{ik_0 z}$, Eq. (5) can be rewritten as

$$\mathcal{A}_{1,zz} + 2ik_0\mathcal{A}_{1,z} + \Delta_\perp\mathcal{A}_1 + \frac{4k_0^2\bar{n}_2}{n_0}|\mathcal{A}_1|^2\mathcal{A}_1 = 0.$$

---

[2] See [6] for the various definitions of the Kerr coefficient.

The scalar nonlinear Helmholtz equation can be further simplified by using the paraxial approximation $|\mathcal{A}_{1,zz}| \ll |k_0 \mathcal{A}_{1,z}|$. The resulting equation for the beam amplitude $\mathcal{A}_1$ is the NLS

$$2ik_0 \mathcal{A}_{1,z} + \Delta_\perp \mathcal{A}_1 + \frac{4k_0^2 \bar{n}_2}{n_0} |\mathcal{A}_1|^2 \mathcal{A}_1 = 0, \tag{6}$$

where $\Delta_\perp = \partial_{xx} + \partial_{yy}$.

2.2. Review of NLS theory

We now give a short review of NLS theory. For more comprehensive presentations, see [20,40]. Let ψ be the solution of the dimensionless NLS

$$i\psi_z + \Delta_\perp \psi + |\psi|^2 \psi = 0, \quad \psi(x, y, z = 0) = \psi_0(x, y). \tag{7}$$

Two important invariants of the NLS (7) are the *power*

$$N(z) = N(\psi(\cdot, z)) := \frac{1}{2\pi} \int |\psi|^2 \, dx \, dy \equiv N(0) \tag{8}$$

and the Hamiltonian

$$H(z) = H(\psi(\cdot, z)) := \frac{1}{2\pi} \left(\int |\nabla_\perp \psi|^2 \, dx \, dy - \frac{1}{2} \int |\psi|^4 \, dx \, dy \right) \equiv H(0). \tag{9}$$

The NLS has the cylindrically symmetric waveguide solution

$$\psi = R(r) \, e^{iz}, \quad r = \sqrt{x^2 + y^2},$$

where $R(r)$, the so-called *Townes soliton*, is the ground-state positive solution of

$$\Delta_\perp R - R + R^3 = 0, \qquad R'(0) = 0, \qquad \lim_{r \to \infty} R(r) = 0. \tag{10}$$

A necessary condition for blowup in the NLS is that the input power be above the critical power N_c [42], i.e., $N(0) \geq N_c$, where N_c is equal to the power of the Townes soliton

$$N_c = \int_0^\infty R^2 r \, dr \approx 1.86. \tag{11}$$

In addition, a sufficient condition for blowup in the NLS is that $H(0) < 0$.

3. Scalar equations with vectorial effects

In this section we identify and use the small parameter f of the model to reduce the vector Helmholtz equation (1) to a scalar equation(s) that takes vectorial and nonparaxial effects into account. The results in this section are as follows (see also Fig. 1). In Section 3.1 we apply perturbation analysis to the vector Helmholtz equation (1) and derive the scalar equation (21). In Section 3.2 we apply a similar perturbation analysis to the Lagrangian (22) of the vector Helmholtz equation, resulting in the Lagrangian (23), whose variational derivative leads to the scalar equation (24). Although Eqs. (21) and (24) are not identical, the two equations agree with each other to the order of accuracy of their derivation (Section 3.2.2). In Section 3.3 we approximate Eq. (21) with (26), which is an initial value problem.
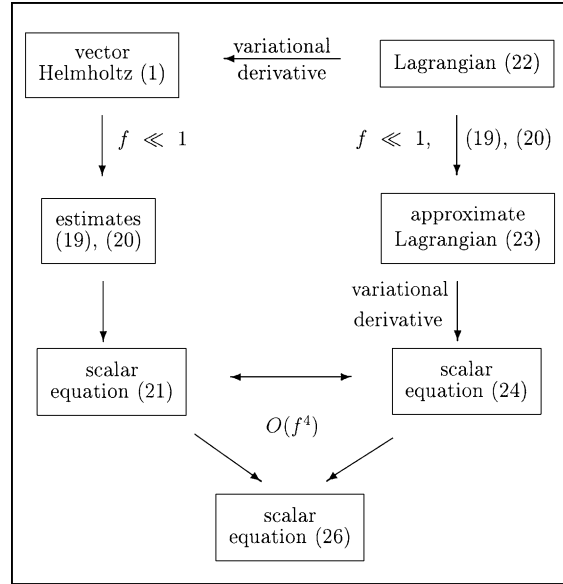
Fig. 1. Schematic outline of the derivation in Section 3.

We note that previous studies [13,16,17] on vectorial effects on self-focusing obtained scalar equations which differ from Eqs. (21), (24) and (26), as well as from each other, in the $O(f^2)$ terms. Because of that, we present in this study a careful systematic derivation of the equations. The agreement of Eqs. (21) and (24), which are derived independently, provides further support that these equations are indeed correct.

3.1. From vector Helmholtz to a scalar equation

The key dimensionless parameter of the model is

$$f = \frac{1}{k_0 r_0} = \frac{\lambda}{2\pi r_0}, \tag{12}$$

where λ is the wavelength and r_0 the input-beam width. Since the wavelength is much smaller than the input-beam width, the parameter f is small, i.e.,

$$f \ll 1. \tag{13}$$

The existence of a small parameter enables us to apply perturbation analysis on Eq. (1) and reduce it to a scalar equation. To do that, we first use Eq. (2) to rewrite Eq. (1) as

$$\Delta \vec{\mathcal{E}} + k_0^2 \vec{\mathcal{E}} + \frac{k_0^2}{\epsilon_0 n_0^2} \vec{\mathcal{P}}_{\mathrm{NL}} = -\frac{1}{\epsilon_0 n_0^2} \nabla(\nabla \cdot \vec{\mathcal{P}}_{\mathrm{NL}}). \tag{14}$$

We rescale the variables according to

$$\tilde{x} = \frac{x}{r_0}, \qquad \tilde{y} = \frac{y}{r_0}, \qquad \tilde{z} = \frac{z}{2L_{\mathrm{DF}}}, \qquad \vec{\mathcal{E}} = \frac{1}{2r_0 k_0} \sqrt{\frac{n_0}{\tilde{n}_2}} \vec{A}(x, y, z)\, \mathrm{e}^{\mathrm{i}k_0 z}, \tag{15}$$

where $\vec{A} = (A_1, A_2, A_3)$ is the dimensionless electric-field amplitude and $L_{DF} = k_0 r_0^2$ the diffraction length. For convenience we drop the tilde signs from now on.

Substitution of (15) in the vector Helmholtz system leads to the dimensionless system

$$i\vec{A}_{,z} + \Delta_\perp \vec{A} + \tfrac{1}{4} f^2 \vec{A}_{,zz} + \vec{N} = -[f\nabla_\perp + \hat{e}_3(i + \tfrac{1}{2} f^2 \partial_z)][f\nabla_\perp \cdot \vec{N} + iN_3 + \tfrac{1}{2} f^2 N_{3,z}], \tag{16}$$

$$f\nabla_\perp \cdot \vec{A} + iA_3 + \tfrac{1}{2} f^2 A_{3,z} = -f^2(f\nabla_\perp \cdot \vec{N} + iN_3 + \tfrac{1}{2} f^2 N_{3,z}), \tag{17}$$

$$\vec{N}(\vec{A}) = \frac{1}{1+\gamma}[(\vec{A} \cdot \vec{A}^*)\vec{A} + \gamma(\vec{A} \cdot \vec{A})\vec{A}^*], \tag{18}$$

where $\hat{e}_3 = (0, 0, 1)$, and $\nabla_\perp = (\partial_x, \partial_y, 0)$. Eqs. (16)–(18) correspond to Eqs. (14), (2) and (3), respectively.

Using a careful perturbation analysis, we show in Appendix A that over propagation distances of several diffraction lengths the dimensionless amplitudes satisfy

$$A_1 = O(1),$$

$$A_2 = O(f^2), \tag{19}$$

$$A_3 = ifA_{1,x} + O(f^3). \tag{20}$$

These relations provide a quantitative measure of the degree to which the beam remains linearly polarized. In particular, relations (19) and (20) indicate that the second transverse component $\mathcal{E}_2$ is significantly smaller than the axial component $\mathcal{E}_3$. The fact that $\mathcal{E}_2/\mathcal{E}_1 = O(f^2)$ plays an important role in the perturbation analysis, because it means that $\mathcal{E}_2$ does not contribute to the perturbation terms in the scalar equations for A_1 (see Appendix B). We note that relation (20) was derived by Lax et. al. [29] under the assumptions that $A_2 \equiv 0$ and that the Kerr effect is "semi-vectorial", i.e., n is given by a relation of the form (4). Thus, the derivation in Appendix A improves on [29] in that relation (19) is proved for a "genuine" vectorial Kerr effect and then used to show that relation (20) remains valid even when $A_2 \not\equiv 0$.

Substituting relations (19) and (20) in the vector Helmholtz equation (16) leads to the following scalar equation for A_1 (Appendix B):

Proposition 3.1. *When $f \ll 1$, Eqs. (1)–(3) can be approximated with the scalar equation*

$$iA_{1,z} + \Delta_\perp A_1 + |A_1|^2 A_1$$
$$= -f^2 \left[\frac{1}{4} A_{1,zz} + \frac{4+6\gamma}{1+\gamma}|A_{1,x}|^2 A_1 + (A_{1,x})^2 A_1^* + \frac{1+2\gamma}{1+\gamma}(|A_1|^2 A_{1,xx} + A_1^2 A_{1,xx}^*)\right] + O(f^4). \tag{21}$$

When $f = 0$, Eq. (21) reduces to the NLS (7). The $A_{1,zz}$ term is the nonparaxial term, which comes from the *scalar* Helmholtz equation (5). The remaining terms on the right-hand side correspond to vectorial effects, i.e., they result from the combined effects of the linear and nonlinear coupling between $\mathcal{E}_1$ and $\mathcal{E}_3$ in Eqs. (1)–(3). Note that $\mathcal{E}_2$ does not contribute to the vectorial terms in Eq. (21), because, in light of Eq. (19), its effect is only $O(f^4)$.

3.2. A variational approach

We now give an alternative derivation of a scalar equation for A_1, based on the Lagrangian of the vector Helmholtz equation (1). It is straightforward to verify that the vector Helmholtz equation (1) has the Lagrangian density

$$\mathcal{L}_{VH}(\vec{\mathcal{E}}, \vec{\mathcal{E}}^*) = \mathcal{E}_{k,k}\mathcal{E}_{j,j}^* - \mathcal{E}_{j,k}\mathcal{E}_{j,k}^* + k_0^2 \mathcal{E}_k \mathcal{E}_k + \frac{2k_0^2 \bar{n}_2}{n_0(1+\gamma)}(\delta_i^l \delta_j^k + \gamma \delta_i^k \delta_j^l)\mathcal{E}_i \mathcal{E}_j^* \mathcal{E}_k \mathcal{E}_l^*, \tag{22}$$

where

$$\mathcal{E}_{i,k} := \frac{\partial \mathcal{E}_i}{\partial x_k}, \qquad \delta_i^j := \begin{cases} 1, & i = j, \\ 0, & i \neq j. \end{cases}$$

The Lagrangian in (22) is written using the standard summation convention. Alternatively, $\mathcal{L}_{VH}$ can also be rewritten as

$$\mathcal{L}_{VH}(\vec{\mathcal{E}}, \vec{\mathcal{E}}^*) = -\sum_{\substack{i,j=1 \\ i \neq j}}^{3} |\mathcal{E}_{i,j}|^2 + k_0^2 |\vec{\mathcal{E}}|^2 + \frac{2k_0^2 \bar{n}_2}{n_0(1+\gamma)} [(\vec{\mathcal{E}} \cdot \vec{\mathcal{E}}^*)^2 + \gamma (\vec{\mathcal{E}} \cdot \vec{\mathcal{E}})^2].$$

Clearly, the quadratic and the quartic terms of $\mathcal{L}_{VH}$ correspond to the linear and nonlinear terms in the vector Helmholtz equation, respectively.

Using the estimates (19) and (20), we show in Appendix C that $\mathcal{L}_{VH}$ can be approximated with terms that depend only on A_1:

$$\mathcal{L}_{A_1}(A_1, A_1^*) = \frac{i}{2}(A_1^* A_{1,z} - A_1 A_{1,z}^*) - |A_{1,x}|^2 - |A_{1,y}|^2 + \frac{1}{2}|A_1|^4$$

$$+ f^2 \left\{ -\frac{1}{4}|A_{1,z}|^2 - |A_{1,xx}|^2 - |A_{1,xy}|^2 + \frac{i}{2}(A_{1,xz}A_{1,x}^* - A_{1,xz}^* A_{1,x}) \right.$$

$$\left. + \frac{1}{2(1+\gamma)}[2|A_1|^2|A_{1,x}|^2 - \gamma((A_{1,x})^2 A_1^{*2} + (A_{1,x}^*)^2 A_1^2)] \right\} + O(f^4). \tag{23}$$

Taking the variational derivative of $\mathcal{L}_{A_1}$ leads to the following equation:

$$iA_{1,z} + \Delta_\perp A_1 + |A_1|^2 A_1 = f^2 \left\{ -\frac{1}{4}A_{1,zz} + \partial_{xx}(iA_{1,z} + \Delta_\perp A_1) - \frac{1}{1+\gamma}[2\gamma|A_{1,x}|^2 A_1 \right.$$

$$\left. - (1+\gamma)(A_{1,x})^2 A_1^* - |A_1|^2 A_{1,xx} + \gamma A_1^2 A_{1,xx}^*] \right\} + O(f^4). \tag{24}$$

Thus, the scalar equation (24) for self-focusing in the presence of vectorial and nonparaxial effects preserves the Lagrangian structure of the vector Helmholtz equation (1).

3.2.1. Invariance

We can use Noether's Theorem to find conservation laws for Eq. (24). Invariance of the action $\int \mathcal{L}_{A_1} \, dx \, dy \, dz$ under phase change $A_1 \rightarrow A_1 \, e^{i\epsilon}$ leads to

$$\int (|A_1|^2 + f^2|A_{1,x}|^2) \, dx \, dy - \frac{i}{4}f^2 \int (A_1 A_{1,z}^* - A_1^* A_{1,z}) \, dx \, dy \equiv \text{const.}$$

This relation can also be obtained by multiplying (24) by A_1^*, subtracting the complex-conjugate and integrating over the (x, y) plane. Clearly, when $f = 0$ this relation reduces to (8). The term $f^2|A_{1,x}|^2$ corresponds to vectorial effects. Indeed, from (19) and (20) we have that

$$\int |\vec{A}|^2 \, dx \, dy = \int (|A_1|^2 + |A_2|^2 + |A_3|^2) \, dx \, dy = \int (|A_1|^2 + f^2|A_{1,x}|^2) \, dx \, dy + O(f^4),$$

which has the meaning of total beam power. The last integral corresponds to nonparaxiality, i.e., it comes from balance of power in the scalar Helmholtz equation (5).

Invariance of the action under "time dilation" $z \to z + \epsilon$ leads to

$$\int \left(|A_{1,x}|^2 + |A_{1,y}|^2 - \frac{1}{2}|A_1|^4 \right) dx\, dy$$

$$- f^2 \int \left\{ -\frac{1}{4}|A_{1,z}|^2 + |A_{1,xx}|^2 + |A_{1,xy}|^2 - \frac{1}{2(1+\gamma)}[2|A_1|^2|A_{1,x}|^2 - \gamma((A_{1,x})^2 A_1^{*2} + (A_{1,x}^*)^2 A_1^2)] \right\} dx\, dy$$

$$\equiv \text{const.}$$

This relation can also be obtained by multiplying (24) by $A_{1,z}^*$, adding the complex-conjugate and integrating over the (x, y) plane.

3.2.2. Consistency of Eqs. (21) and (24)

The two scalar equations for A_1, Eqs. (21) and (24), are derived from the same 'mother' equation and by using the same assumptions and approximations. In both Eqs. (21) and (24), the O(1) and nonparaxial terms are the same, but the $O(f^2)$ terms that come from vectorial effects are not. This apparent inconsistency can be resolved by showing that the two equations differ only by $O(f^4)$ terms, which is the order of accuracy of these equations:

Proposition 3.2. *Eqs.* (21) *and* (24) *differ only by* $O(f^4)$ *terms.*

Proof. see Appendix D.   □

Indeed, we note that if we use the vector Helmholtz equation in the form (1) instead of (14) in the derivation in Appendix B, then the perturbation analysis will lead to Eq. (24), rather than to Eq. (21).

3.3. Initial value problem

Both Eqs. (21) and (24) contain the nonparaxial term $A_{1,zz}$. This term is not related to vectorial effects, as it comes from substitution of the ansatz $\mathcal{E}_1 = \mathcal{A}_1(x, y, z)\, e^{ik_0 z}$ in the *scalar* nonlinear Helmholtz equation (5). Because the Helmholtz equation is a boundary-value problem, solving it numerically on the half-plane $z \geq 0$ requires setting appropriate radiation boundary conditions at $z \to \infty$. Since, in addition, this equation is nonlinear, solving it as a true boundary-value problem is difficult. [3] Therefore, the standard approach in numerical simulations is to approximate the nonparaxial term $A_{1,zz}$ with terms that do not have z-derivatives. In Appendix E we show that the nonparaxial term in Eqs. (21) and (24) can be approximated with

$$A_{1,zz} = -[\Delta_\perp^2 A_1 + 4|A_1|^2 \Delta_\perp A_1 + 4(\nabla_\perp A_1) \cdot (\nabla_\perp A_1^*)A_1 + 2(\nabla_\perp A_1) \cdot (\nabla_\perp A_1)A_1^* + |A_1|^4 A_1] + O(f^2), \tag{25}$$

where $\Delta_\perp^2 := (\partial_{xx} + \partial_{yy})^2$ is the biharmonic operator. Substituting the approximation (25) in Eq. (21) leads to the

---

[3] For a recent numerical study of the scalar nonlinear Helmholtz equation as a true boundary-value problem, see [22].

following initial value problem:

$$\underbrace{iA_{1,z} + \Delta_\perp A_1 + |A_1|^2 A_1}_{\text{NLS}}$$

$$= \underbrace{\tfrac{1}{4} f^2 [\Delta_\perp^2 A_1 + 4|A_1|^2 \Delta_\perp A_1 + 4(\nabla_\perp A_1) \cdot (\nabla_\perp A_1^*) A_1 + 2(\nabla_\perp A_1) \cdot (\nabla_\perp A_1^*) A_1^* + |A_1|^4 A_1]}_{\text{nonparaxial}}$$

$$\underbrace{\times - f^2 \left[\frac{4+6\gamma}{1+\gamma} |A_{1,x}|^2 A_1 + (A_{1,x})^2 A_1^* + \frac{1+2\gamma}{1+\gamma}(|A_1|^2 A_{1,xx} + A_1^2 A_{1,xx}^*) \right]}_{\text{vectorial}} + O(f^4). \tag{26}$$

For convenience, we note the origin of the terms in Eq. (26).

Clearly, all three scalar equations for A_1 agree with each other to the order of their accuracy:

Corollary 3.1. *Eqs. (21), (24) and (26) differ only by* $O(f^4)$ *terms.*

4. Vectorial effects and multiple filamentation

In self-focusing experiments, a sufficiently intense laser beam can break-up into several long and narrow filaments, a phenomenon known as multiple filamentation [1,3,7–9,11,12,14,15,28,30,36–38]. According to the NLS model, however, if the input beam is cylindrically symmetric, then the beam should remain cylindrically symmetric during propagation. Therefore, in order to explain the phenomenon of multiple filamentation, where cylindrical symmetry is clearly lost, one has to add a symmetry-breaking mechanism to the NLS model. The standard explanation for multiple filamentation (see Section 6.2), is that breakup of cylindrical symmetry is initiated by *random* noise in the input beam. We now show that *deterministic* vectorial effects can also lead to multiple filamentation.

In order to understand why vectorial effects might lead to multiple filamentation, we note that the asymmetry in the x and y derivatives of the vectorial perturbation terms in either Eq. (21), (24) or (26) implies that vectorial effects are a symmetry-breaking mechanism. Clearly, this, by itself, does not imply that vectorial effects lead to multiple filamentation. However, the following simulations show that when the input beam is sufficiently powerful, vectorial effects do lead to multiple filamentation.

We note that at present there is no theory for the NLS in the high-power regime $N(0) \gg N_c$. Therefore, our results in this high-power regime on vectorial effects in general, and on multiple filamentation in particular, are only numerical. The arrest of collapse and the focusing–defocusing oscillations that are observed in the following simulations have some theoretical basis, which is discussed in Section 5.

We begin by presenting the results of simulations of Eq. (26) with $f = 0.05$ and $\gamma = \tfrac{1}{2}$, where we gradually increase the input power $N(0)$. The input beam is a cylindrically symmetric Gaussian,

$$A_1(x, y, z = 0) = 2\sqrt{N(0)}\, e^{-(x^2+y^2)}, \tag{27}$$

where the constant $N(0)$ is equal to the input power of A_1.

When $N(0) = 2N_c$, the beam propagates as a single filament which undergoes focusing–defocusing oscillations (Figs. 2 and 3). Although the beam appears to be symmetric during its propagation, a more careful inspection shows a small deviation from cylindrical symmetry.

When $N(0) = 3N_c$, the beam initially goes through the following stages: (i) self-focusing, (ii) defocusing into a symmetric ring (crater), (iii) second self-focusing, (iv) defocusing and formation of two small sub-peaks, and (v) focusing with a single peak (Fig. 4). During further propagation, the beam undergoes focusing–defocusing oscillations (Fig. 5).
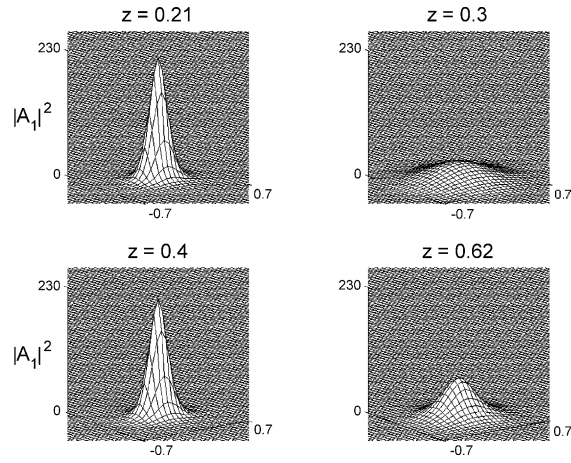
Fig. 2. Solution of Eq. (26) with the input beam (27), $f = 0.05$, $\gamma = 0.5$, and $N(0) = 2N_c$.
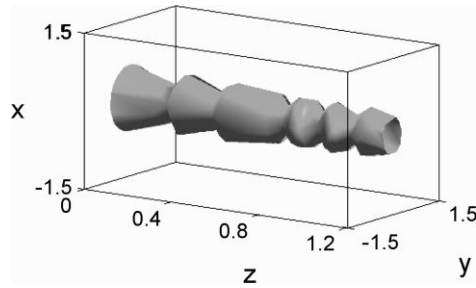

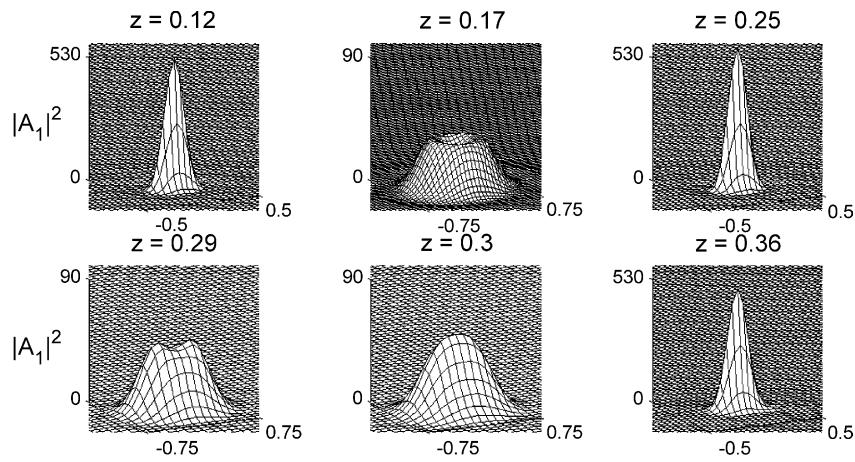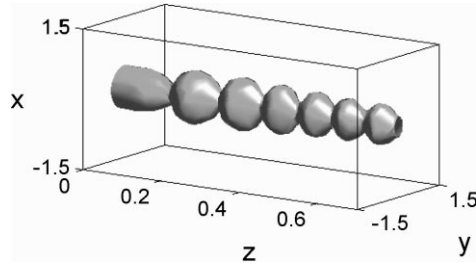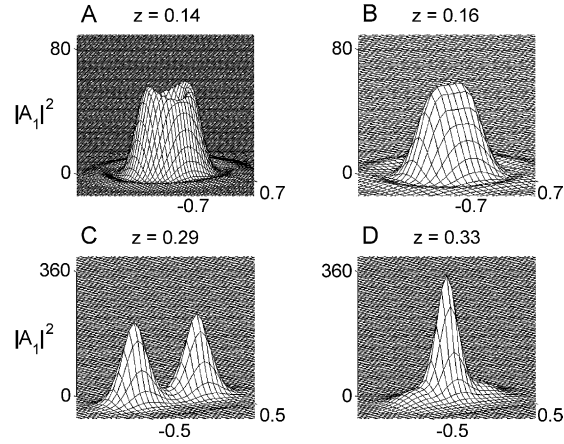Fig. 3. Iso-surface $|A_1|^2 \equiv 7$ of the data in Fig. 2.


Fig. 4. Same as Fig. 2 with $N(0) = 3N_c$.

Fig. 5. Iso-surface $|A_1|^2 \equiv 15$ of the data in Fig. 4.

Fig. 6. Same as Fig. 2 with $N(0) = 3.75N_c$.

When the input power is raised to $N(0) = 3.75N_c$, the beam initially self-focuses and defocuses into an asymmetric ring with two peaks on its rim (Fig. 6). After the second focusing–defocusing cycle, a complete breakup of cylindrical symmetry occurs as the beam splits into two filaments. Shortly after, however, the two filaments reunite and continue to propagate as a single filament, as can be seen in Fig. 7. We call this phenomenon *pseudo-multiple filamentation*, in order to distinguish it from (genuine) multiple filamentation, in which the filaments do not reunite.
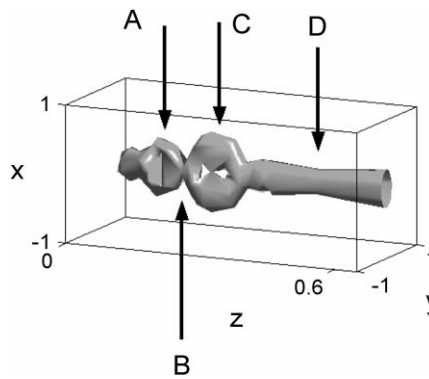
Fig. 7. Iso-surface $|A_1|^2 \equiv 48$ of the data in Fig. 6. Capital letters mark the corresponding z-slices on the 3D plots in Fig. 6.
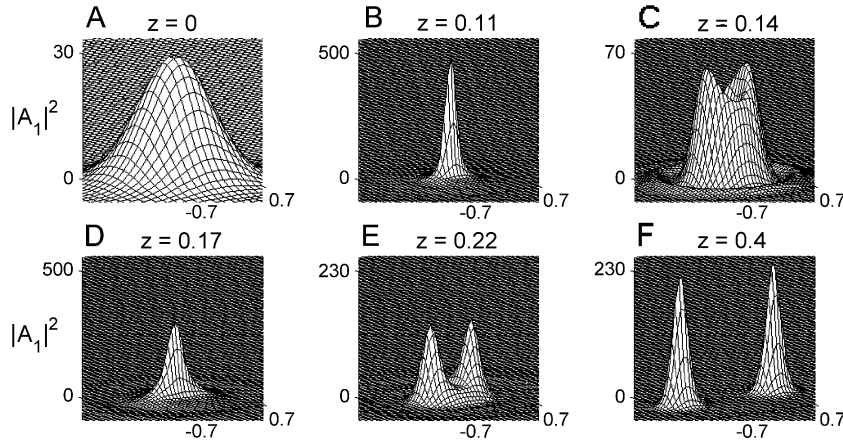
Fig. 8. Same as in Fig. 2 with $N(0) = 4N_c$. Viewing angle in the (x, y) plane is $-35°$.

As the input power is further increased to $N(0) = 4N_c$, a similar dynamics leads to the emergence of two filaments (Fig. 8). This time, however, the two filaments do not reunite. Rather, they propagate forward in the z direction, while moving away from each other along the x-axis (Fig. 9). When the power is increased to $N(0) = 10N_c$, the beam goes through the same stages, but in this case the two filaments move away from each other along the y-axis (Figs. 10 and 11).

We note that vectorial effects induce a preferred direction in the transverse (x, y) plane: The direction on initial polarization (the x-axis direction in our model). Therefore, in the case of cylindrically symmetric input beams, when vectorial effects lead to breakup of the beam into two filaments, the two filaments can move away from each other (in the transverse plane) either along the direction of initial polarization (as in Fig. 9) or perpendicular to it (as in Fig. 11).

Finally, with $N(0) = 20N_c$ we observe multiple filamentation into five filaments: One that continues to propagate along the z-axis and four other filaments that propagate slightly 'sideways' (Figs. 12 and 13).

We now vary some other parameters in the simulations. In Fig. 14 we add a focusing lens at the medium's interface $z = 0$ to the input beam of Fig. 6, i.e., the initial condition is

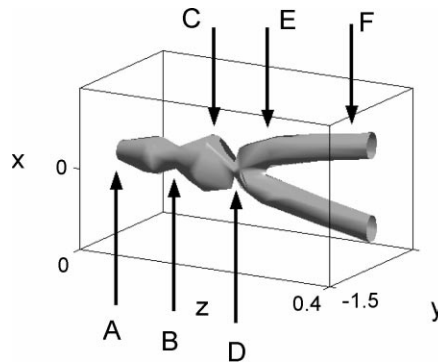$$A_1(x, y, z = 0) = 2\sqrt{2N(0)}\, e^{-(x^2+y^2)}\, e^{-i(x^2+y^2)/4}, \tag{28}$$
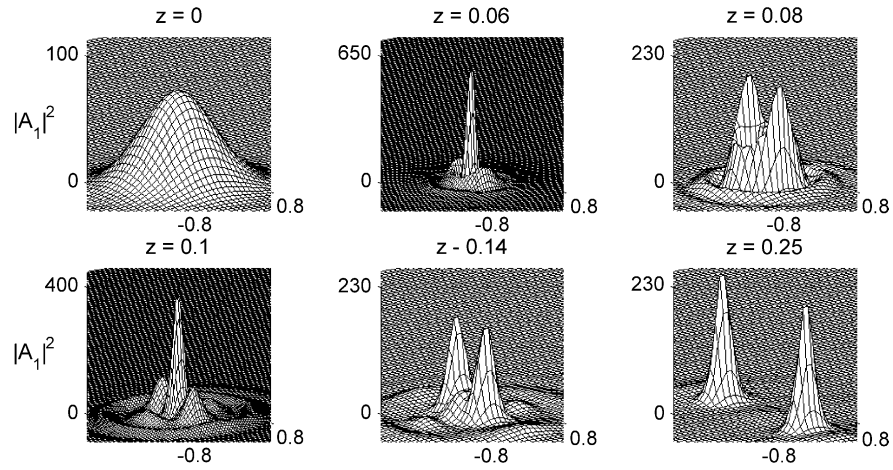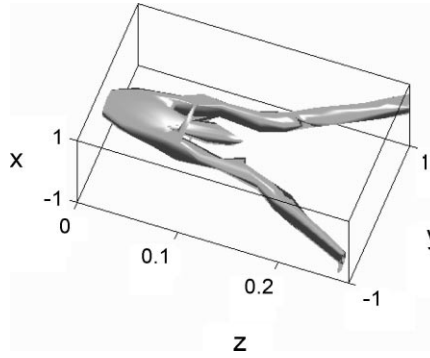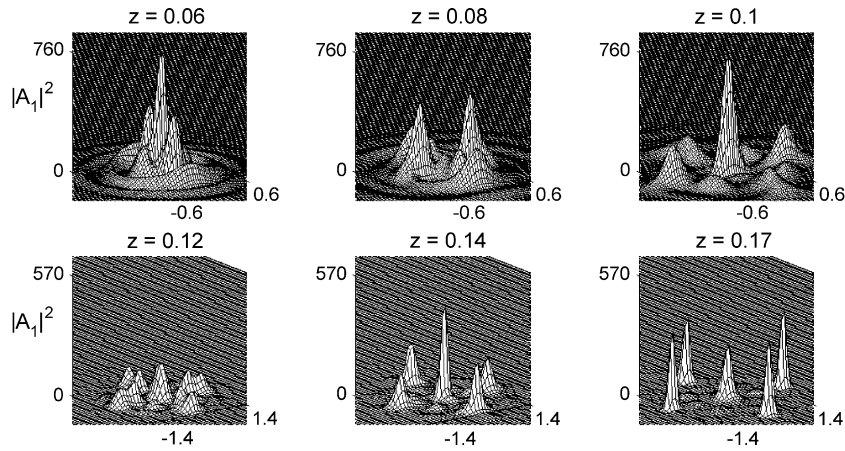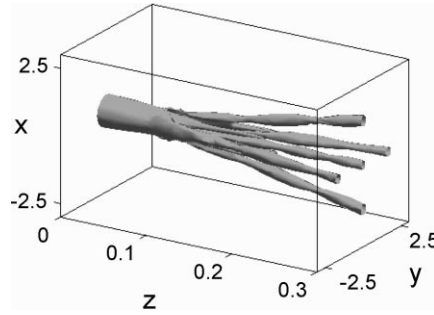

Fig. 9. Iso-surface $|A_1|^2 \equiv 30$ of the data in Fig. 8.

Fig. 10. Same as Fig. 2 with $N(0) = 10N_c$.

Fig. 11. Iso-surface $|A_1|^2 \equiv 70$ of the data in Fig. 10.

Fig. 12. Same as Fig. 2 with $N(0) = 20N_c$. Viewing angle in the (x, y) plane is $-35°$.
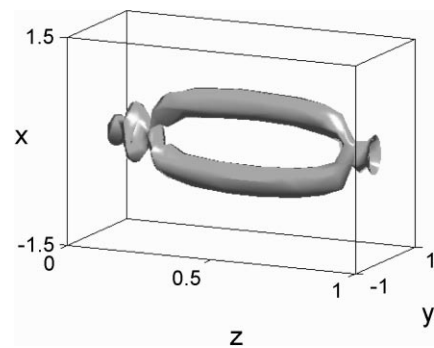
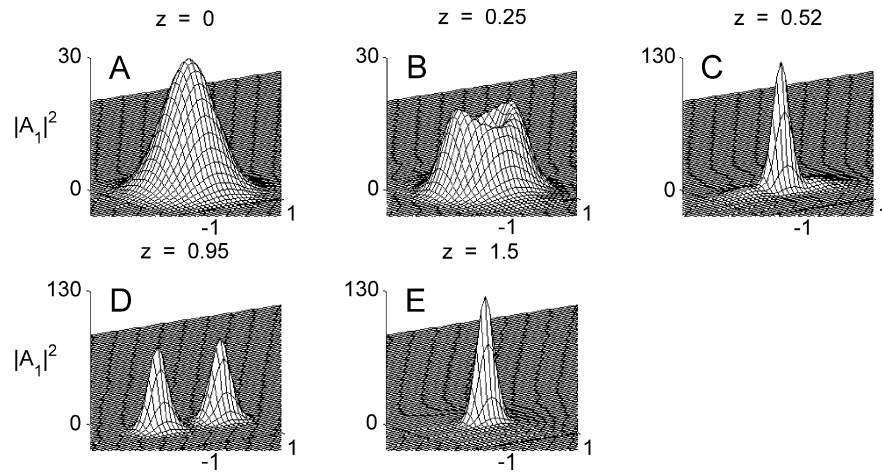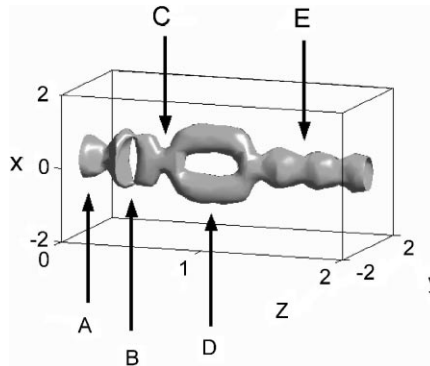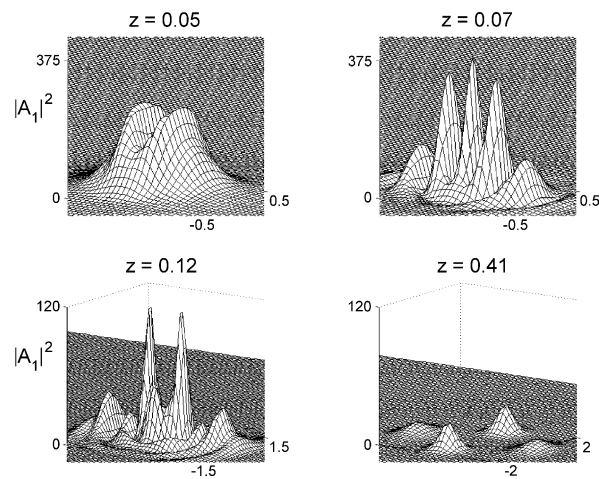Fig. 13. Iso-surface $|A_1|^2 \equiv 50$ of the data in Fig. 12.

and $N(0) = 3.75N_c$. In this simulation we observe the same qualitative dynamics as with the unfocused beam, except that the pseudo-multiple-filamentation stage is much longer.

In Figs. 15 and 16 we repeat the simulation of Fig. 8 with $f = 0.1$. In this case we observe pseudo-multiple filamentation, rather than a genuine one. We do, however, observe genuine multiple filamentation for $f = 0.1$ when $N(0) = 5N_c$. Therefore, the threshold power for multiple filamentation is higher for $f = 0.1$ than for $f = 0.05$. This result is surprising, since a larger f corresponds to stronger vectorial effects. In Figs. 17 and 18 we repeat the simulations of Figs. 12 and 13 with $f = 0.08$. In this case, the beam splits into four filaments, all of which propagate slightly off the z-axis.

Although there is still no complete picture of vectorial effects on self-focusing, the above simulations, as well as additional ones which we do not show, suggest the following. For given model parameters, there is a threshold power for genuine multiple filamentation (which appears to be in the range $3N_c$–$5N_c$), such that,

1. When the input-power is sufficiently below this threshold, the beam propagates as a single filament, undergoing focusing–defocusing oscillations.
2. When the input-power is slightly below the threshold, an asymmetric ring is formed during the defocusing stage, followed by pseudo-multiple filamentation.
3. When the input-power is moderately above the threshold, an asymmetric ring is formed during the defocusing stage, followed by beam splitting into two disjoint filaments (genuine multiple filamentation).
4. When the input-power is highly above the threshold, the beam can split into more than two filaments. In this case,

Fig. 14. Iso-surface $|A_1|^2 \equiv 45$ of the same data as in Fig. 6 with a focusing lens (i.e., the initial condition (28)).

z = 0   z = 0.25   z = 0.52

z = 0.95   z = 1.5

Fig. 15. Same as Fig. 8 with $f = 0.1$.

Fig. 16. Iso-surface $|A_1|^2 \equiv 15$ of the data in Fig. 15.

z = 0.05   z = 0.07

z = 0.12   z = 0.41

Fig. 17. Same as Fig. 12 with $f = 0.08$. Viewing angle in the (x, y) plane of the 3D graphs is $-55°$.
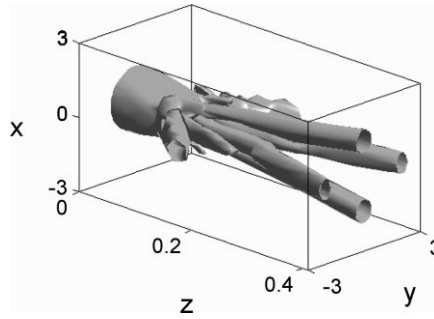
Fig. 18. Iso-surface $|A_1|^2 \equiv 5$ of the data in Fig. 17.

all filaments split from the central beam (rather than a fractal process where the beam splits into two filaments and then each filament splits again).

In both (3) and (4) all filaments are of comparable power, which is roughly between $1.5N_c$ and $3.6N_c$. Thus, the power of each filament is below the threshold for additional splitting.

As we have already said, vectorial effects play an essential role in the multiple filamentation in Figs. 8–13, as they are the only mechanism that breaks-up the axial-symmetry. Because nonparaxiality preserves axial-symmetry, a natural question is whether it is 'needed' for multiple filamentation. To answer this question, we repeat the simulations of Figs. 8–13 but without the nonparaxial terms. In these simulations we observe some breakup of axial-symmetry but not multiple filamentation. Therefore, it is possible that nonparaxiality is also needed for multiple filamentation.

We remark that in the iso-intensity plots of multiple filamentation (Figs. 9, 11 and 13), the filaments are not parallel to each other. Rather, there is an angle of several degrees between the filaments. Such an angle has neither been reported in the multiple filamentation experiments literature, nor in previous numerical studies, where noise in the input beam leads to multiple filamentation. This may suggest that multiple filamentation due to noise is more similar to experimental observations than multiple filamentation due to vectorial effects. This is not the case, however, because of the following reasons:

1. Most experiments of multiple filamentation measure the beam intensity at a fixed z. Therefore, it is possible that such an angle went unnoticed.
2. Because of the different rescaling in the axial and transverse coordinates (see Eq. (15)), the physical angle is approximately f times the angle in our iso-intensity plots. Thus, the physical angle is much smaller than what appears in the plots.
3. In our simulations of noise-driven multiple filaments in Section 6, these filaments are also not parallel (see Fig. 24).

5. Modulation theory for vectorial effects

The numerical simulations in Section 4 show that when the input beam is sufficiently powerful, vectorial effects can lead to multiple filamentation. In addition, these simulations show that, regardless of whether multiple filamentation occurs or not, beam collapse is arrested and a single filament or several filaments are formed, which propagate over long distances while maintaining roughly a constant width.

At present there is no theory for analyzing self-focusing in the high-power regime $N(0) \gg N_c$, which is why we rely on numerical simulations in the exploration of multiple filamentation. However, when the power of a single

filament is not much higher than N_c, its propagation can be analyzed using *modulation theory*, which is an asymptotic theory for analyzing the effects of small perturbations on critical self-focusing [20,21]. Modulation theory is based on the observation that, after some propagation has taken place, a self-focusing filament rearranges itself as a modulated Townesian, i.e., $|A_1| \sim L^{-1}(z)R(r/L(z))$, where $R(r)$ is defined in Eq. (10). Therefore, self-focusing dynamics is described by the modulation variable $L(z)$, which is proportional to beam-width and also to 1/(on-axis amplitude). In particular, $L \to 0$ and $L \to \infty$ correspond to blowup and to complete defocusing, respectively.

By applying modulation theory to Eq. (21) we prove in Appendix F that

Proposition 5.1. *When* $f \ll 1$, *the self-focusing dynamics of a single filament propagating in the presence of vectorial and nonparaxial effects (i.e., Eq. (21)) is given, to leading order, by the reduced system of ODEs*

$$L_{zz}(z) = -\frac{\beta}{L^3}, \qquad \beta_z(z) = -\frac{f^2(C_{np} + C_{vec})N_c}{2M}\left(\frac{1}{L^2}\right)_z, \tag{29}$$

where

$$M = \frac{1}{4}\int_0^\infty \rho^2 R^2 \rho\,d\rho \approx 0.55, \tag{30}$$

$$C_{np} = 1 \quad and \quad C_{vec}(\gamma) \approx \frac{16}{3}\left(1 + \frac{\gamma}{1+\gamma}\right). \tag{31}$$

Inspection of the derivation of Eq. (29) shows that the terms with C_{np} and with C_{vec} correspond to nonparaxial and vectorial effects, respectively. Therefore, the reduced system (29) shows that nonparaxiality and vectorial effects have the same qualitative effect on self-focusing dynamics of a single filament. This observation is surprising, because at the PDE level (i.e., Eq. (21)) the expressions for nonparaxiality and for vectorial effects are completely different. It is interesting to note that the reduced system (29) also appears in the study of self-focusing dynamics with a saturated-nonlinearity effect [19–21], such as Eq. (36).

As can be seen from Table 1, $\gamma \geq 0$ for most common physical mechanisms leading to the Kerr effect. Therefore, from (31) we have that $C_{vec}(\gamma) \geq \frac{16}{3}$. Thus, the reduced system (29) shows that vectorial effects dominate over nonparaxiality. This observation implies that models of physical self-focusing which include nonparaxiality should also include vectorial effects. We note that this has not been done in most previous studies.

We can follow [19,21] and integrate Eqs. (29) to get

$$(y_z)^2 = -\frac{4H_0}{My}(y_M - y)(y - y_m), \quad y(z) := L^2(z), \tag{32}$$

where

$$y_m \approx \frac{M\beta(0)}{-2H_0}(1 - \sqrt{1 - 4\delta}) \sim \frac{f^2 N_c(C_{np} + C_{vec})}{4M\beta(0)}[1 + O(\delta)],$$

$$y_M \approx \frac{M\beta(0)}{-2H_0}(1 + \sqrt{1 - 4\delta}) \sim \frac{M\beta(0)}{-H_0}[1 + O(\delta)], \tag{33}$$

$\delta = -f^2 N_c(C_{np} + C_{vec})H_0/4M^2\beta^2(0)$ and $H_0 \approx H(0)$.

We recall that a necessary condition for blowup in the unperturbed NLS, i.e., Eq. (6), is that the input power is above critical, i.e., $N(0) > N_c$ (see Section 2.2). In modulation theory variables [21], this condition amounts to $\beta(0) \approx (N(0) - N_c)/M > 0$. However, when $\beta(0) > 0$ we see from Eqs. (32) and (33) that $y(z) \geq y_m > 0$. Therefore blowup is arrested by vectorial and nonparaxial effects and the minimal beam width is $L_m \sim$
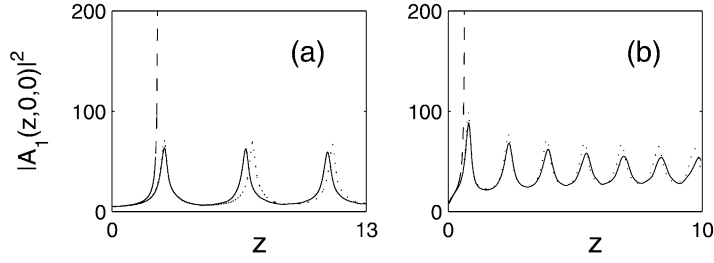
Fig. 19. Blowup in NLS (i.e., Eq. (6), dashed line) is arrested by vectorial effects, with nonparaxiality (i.e., Eq. (26), solid line) and without nonparaxiality (i.e., setting $A_{1,zz} \equiv 0$ in Eq. (21), dots), resulting instead in focusing–defocusing oscillations. Here $f = 0.04$, $\gamma = 0.5$, and (a) $A_1(z = 0, r) = \sqrt{1.05}R(r)$ (i.e., $N(0) = 1.05N_c$); (b) $A_1(z = 0, r) = 2\sqrt{1.1N_c}\,e^{-r^2}$ (i.e., $N(0) = 1.1N_c$).

$L(0)f\sqrt{N_c(C_{np} + C_{vec})/4M\beta(0)}$, which, in physical variables, corresponds several wavelengths. Even at this stage the magnitude of the nonparaxial and vectorial terms in Eq. (21) is $O(\beta)$ smaller than that of the NLS terms $\Delta_\perp A_1$ and $|A_1|^2 A_1$, providing an a posteriori justification for treating them as small perturbations.

In addition, a sufficient condition for blowup in the unperturbed NLS (6) is $H(0) < 0$. However, from Eqs. (32) and (33) we see that if $\beta(0) > 0$ and $H(0) < 0$ then $y_m \leq y(z) \leq y_M$, i.e., arrest of blowup is followed by focusing–defocusing oscillations. When nonadiabatic radiation is added to (29) the oscillations decay with propagation [19].

The qualitative picture predicted by (29), i.e., arrest of blowup followed by focusing–defocusing oscillations, can be observed in the simulations of Fig. 19 where the input power is only moderately above N_c, as well as in previous numerical studies of vectorial effects [24,25]. We also verified the prediction of the reduced system (29) that the effect of nonparaxiality is small compared with that of vectorial effects, by comparing in Fig. 19 the dynamics with and without nonparaxial effects. Finally, we verified that if nonparaxial effects are kept but vectorial effects are
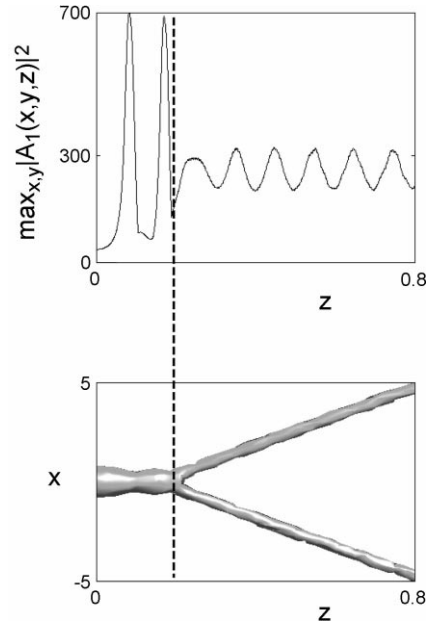

Fig. 20. Same as Fig. 2 with $N(0) = 5N_c$. Top: peak intensity. Bottom: iso-surface $|A_1|^2 = 10$.

neglected in the simulations of Fig. 19 then the qualitative dynamics remains the same but the peak intensities are significantly higher.

When the input power is above the threshold for multiple filamentation, a more careful inspection of the data in Figs. 8,10 and 12 reveals that after the splitting has taken place each filament undergoes almost-periodic focusing–defocusing oscillations. For example, in Fig. 20 multiple filamentation occurs after the first two oscillations, and the subsequent oscillations are the focusing–defocusing cycles of each filament.

As in the case of the angle between the filaments (see remark at the end of Section 4), in physical variables the oscillations are much slower than what may appear from Figs. 3,5,16–19 and 20. These focusing–defocusing oscillations can be interpreted as self-trapping, i.e., the formation of a long and narrow filament. Indeed, such oscillations were observed in the cw self-trapping experiments of Bjorkholm and Ashkin [5].

6. Randomness and multiple filamentation

6.1. The Bespalov–Talanov model

In 1966, Bespalov and Talanov [4] suggested that noise in the input beam is the symmetry-breaking mechanism that leads to multiple filamentation. Their analysis was based on the assumption that, to leading order, the electric field is a plane-wave, i.e.,

$$\mathcal{E}_1(x, y, z) \sim \alpha \, e^{-i\alpha^2 z}, \quad \alpha \equiv \text{const.} \tag{34}$$

Using this assumption, they showed that certain frequencies are linearly unstable. From this they concluded that instabilities would breakup the cylindrical symmetry of the beam, leading ultimately to multiple filamentation.

To test numerically the Bespalov–Talanov model for multiple filamentation, we solve the unperturbed NLS (6) with a high-power ($N(0) \gg N_c$) cylindrically symmetric Gaussian input beam, to which we add random noise both in amplitude and in phase, i.e.,

$$A_1(x, y, z = 0) = c_1 \, e^{-(x^2+y^2)}[1 + c_2 \, \text{noise}(x, y)], \tag{35}$$

where c_1 is a constant, noise(x, y) a random complex-valued function, and the constant c_2 determines the noise level ($c_2 \ll 1$). Although we have made many simulations with high-power input beams and random noise, we see neither evidence for multiple filamentation nor even mild instabilities. Rather, the beam converges to a cylindrically symmetric profile as it blows-up (see Fig. 21).
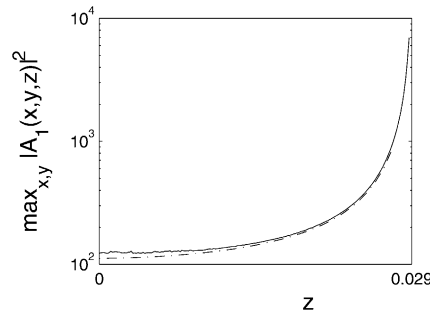

Fig. 21. Blow-up in the NLS (6) of high-power input beams (35) with noise (solid line, $c_2 = 0.1$) and in the absence of noise (dot-dashed line, $c_2 = 0$) is very similar. Here $c_1 = 2\sqrt{15N_c}$ (i.e., $N(0) \approx 15N_c$).

Apparently, the major weakness of the Bespalov–Talanov argument is that it assumes that, to leading order, the electric field is a plane-wave (34). Under this assumption (which implies infinite input power) the self-focusing process of the field does not depend on the transverse dynamics, i.e., $\mathcal{E}_{1,z} + |\mathcal{E}_1|^2 \mathcal{E}_1 = 0$. As a result, instabilities can grow while the leading order solution remains unchanged. This is not the case, however, for a propagating beam, where the transverse dynamics of the beam dominates the evolution of the noise.

6.2. Noise and a saturating nonlinearity

In 1968, Marburger and Dawes [34] showed numerically that intense Gaussian beams propagating in a Kerr medium with saturable nonlinearity do not collapse, but instead go through focusing–defocusing cycles. In addition, they showed that the transverse profile of the beam can develop a concentric ring structure. Although they pointed out the relation between a ring structure and the formation of small-scale filaments, they could not demonstrate this numerically, because their code was cylindrically symmetric. This relation was established in 1979, when Konno and Suzuki [27] solved the saturated NLS using a Cartesian grid and showed that the ring structure is indeed unstable. Later, using both numerics and an approximate stability analysis, Soto-Crespo et al. [39] showed that the transition from cylindrical symmetry to multiple filamentation is associated with the appearance of a spatial ring. Multiple filamentation due to noise in the input beam and nonlinear saturation was also observed in [2,23,33,35,41].

In order to compare multiple filamentation due to vectorial effects with the one to noise, we solve the saturated NLS

$$iA_{1,z} + \Delta_\perp A_1 + \frac{|A_1|^2 A_1}{1 + \epsilon |A_1|^2} = 0, \quad 0 < \epsilon \ll 1 \tag{36}$$

with high-power noisy input beams (35). For example, when $\epsilon = 0.01/\ln 2$ and $c_2 = 0.02$, we observe pseudo-multiple filamentation when $N_0 \approx 10N_c$ (Fig. 22) and genuine multiple filamentation when $N_0 \approx 15N_c$ (Figs. 23 and 24). Therefore, for these values of ϵ and c_2, the threshold for multiple filamentation lies between $10N_c$ and $15N_c$.

We carry additional simulations of Eq. (36) with the same values of ϵ and c_2 in the range $15N_c \le N(0) \le 120N_c$. These simulations suggest that noise-induced multiple filamentation is characterized by a powerful central on-axis filament, from which less-powerful off-axis filaments split. After multiple filamentation occurs, above half the input power remains in the on-axis filament. The off-axis filaments are less powerful, as the power of each is below
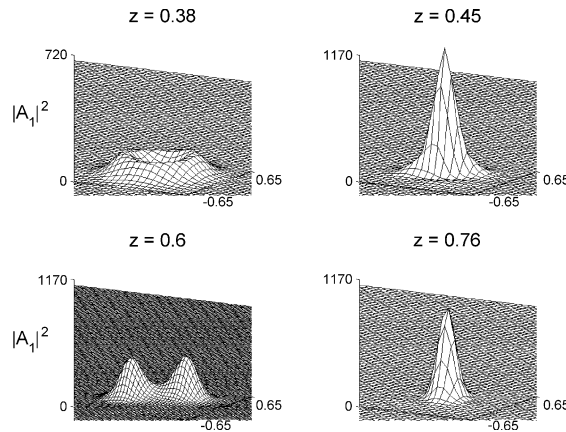

Fig. 22. Solution of Eqs. (36) with $\epsilon = 0.01/\ln 2$ with the input beam (35), where $c_1 = 7.5/\sqrt{\ln 2}$ (i.e., $N(0) \approx 10N_c$) and $c_2 = 0.02$.
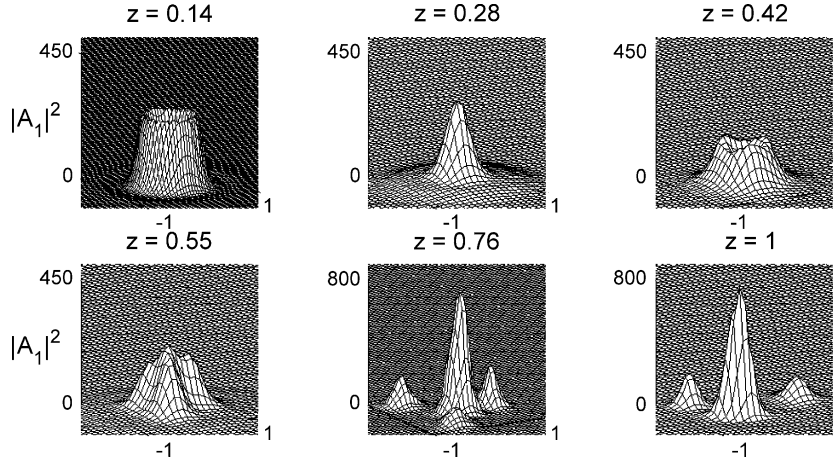
Fig. 23. Same as Fig. 22 with $c_1 = 9/\sqrt{\ln 2}$ (i.e., $N(0) \approx 15N_c$).
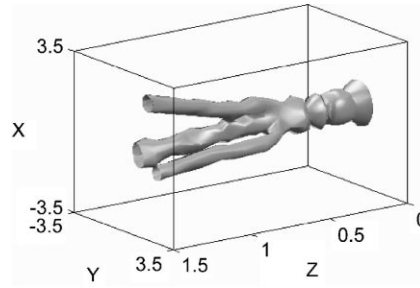

Fig. 24. Iso-intensity surface $|A_1|^2 = 30$ of the data in Fig. 23. Note that the beam propagates from right to left.

one-tenth of the input power. In addition, a significant amount of power is radiated to the background, as was also observed in [41]. We note that even when the power of the on-axis filament is much larger than $15N_c$ (i.e., above the initial threshold for multiple filamentation), no additional splitting occurs. This observation shows that, as can be expected, the effect of input noise diminishes with propagation.

We note that saturation of the Kerr nonlinearity has been observed experimentally for only some materials. For example, Yau, Lee and Wang reported recently that the nonlinearity for sapphire crystal is of the form (36). However, there are other materials for which the assumption of nonlinear saturation does not have a solid physical justification. Therefore, a natural question is whether noise can lead to multiple filamentation in the absence of saturation. To address this question, we note that nonparaxiality, which is always present, can also play the role of a stabilizing mechanism which leads to the formation of rings. In addition, the simulations of Feit and Fleck [18] suggest that a ring structure is unstable in the NLS with nonparaxiality but with no saturation, and that it breaks into multiple filaments. Therefore, it is possible that the addition of nonlinear saturation is not really needed in order for noise to lead to multiple filamentation.

7. Vectorial effects or noise?

As we have seen, regardless of whether the symmetry-breaking mechanism is vectorial effects or noise in the input beam, multiple filamentation always occurs after the formation of a ring during the defocusing stage.

Because a ring structure is unstable, it can be broken into multiple filaments by symmetry-breaking mechanisms.

There are, however, significant differences between multiple filamentation induced by vectorial effects and by noise. The most important difference is that the former is a deterministic process whereas the latter is a random one. Therefore, when the input beam is cylindrically symmetric ('clean' input beam) the filamentation pattern is reproducible in the case of vectorial-induced filaments but varies from experiment to experiment in the case of noise-induced filaments. Another difference, which can be utilized to determine experimentally the mechanism of multiple filamentation (see Section 8) is that vectorial effects induce a preferred direction in the transverse (x, y) plane, which is the direction of input-beam polarization.

Our simulations suggest that the threshold power for multiple filamentation caused by vectorial effects is significantly lower than the one for multiple filamentation caused by noise. For example, simulations of Eq. (36) with $\epsilon = 0.01$ and noise level of $c_2 = 0.02$ do not lead to multiple filamentation when $N(0) < 10N_c$, but do lead to multiple filamentation when $N(0) > 15N_c$. In contrast, in the vectorial case with $f = 0.05$, we already observe multiple filamentation when $N(0) = 4N_c$. Thus, multiple filamentation at these lower powers is more likely to be the result of vectorial effects.

Another difference is that in vectorial-induced multiple filamentation, regardless of whether there is a central filament after the splitting (Fig. 12) or not (Fig. 8), all filaments are of comparable power, which is below $3.6N_c$. In contrast, noise-induced multiple filamentation is characterized by a powerful central filament which has about half the input power, and significantly less-powerful off-axis filaments.

8. An experimental test

The results presented so far show that multiple filamentation can result from either vectorial effects or from noise in the input beam. Therefore, in theory, when all parameters of a multiple-filamentation experiment are known, one can use numerical simulations to determine whether the mechanism behind multiple filamentation is vectorial effects or noise. However, at the high input powers associated with multiple filamentation, other physical mechanisms (e.g., plasma generation, time-dispersion, etc.), which are neglected in both models, can also become important. Thus, our model might not capture all the relevant physics, in which case, its reliability in determining the mechanism behind multiple filamentation is less clear.

In order to overcome this difficulty and be able to determine whether vectorial or random effects are the physical mechanism behind multiple filamentation, we propose the following experimental test. This test is based on the observation that *vectorial effects are the only mechanism neglected in the derivation of the NLS model that breaks-up the cylindrical symmetry while inducing a preferred direction* in an isotropic homogeneous medium (the direction of input-beam polarization). Therefore, if multiple filamentation is caused by vectorial effects, then

1. The filamentation pattern in the transverse plane should persist between experiments.
2. When the direction of linear polarization of the input beam is rotated in the transverse plane between experiments, the filamentation pattern should follow the same rotation.
3. When a beam splits into two filaments, the splitting should occur either along the direction of initial polarization or perpendicular to it (see Figs. 9 and 11).

In contrast, when multiple filamentation results from random instabilities, the filamentation pattern should vary between experiments and be independent of the direction of initial polarization.

We note that in the multiple-filamentation experiments in [36], Nowak and Ham observed that "the . . . [filament] patterns. . . , although random in appearance, were perfectly reproducible shot to shot" (a similar observation was

Table 2
Mesh size and computational domain $(x, y) \in [0, X_{max}] \times [0, Y_{max}]$ used in simulations of Figs. 2–18

Figure	$\mathrm{d}x = \mathrm{d}y$	X_{max}, Y_{max}
2 and 3	0.06	7.5, 7.5
4–7 and 14	0.05	8, 8
8 and 9	0.055	8, 8
10 and 11	0.04	7, 7
12 and 13	0.03	8, 12
15 and 16	0.05	7, 7
17 and 18	0.045	8, 16

reported by Brodeur et al. [9]). Because of this observation, Nowak and Ham conjectured that multiple filamentation was due to small inhomogeneities in the medium. However, our study shows that this behavior is also consistent with the vectorial effects explanation for multiple filamentation.

9. Numerical methods

In our simulations of the $(2 + 1)$D Eqs. (7), (26) and (36), we use a finite-difference scheme on a rectangular Cartesian grid (see Table 2) with fourth-order accuracy in space. Time-stepping (i.e., z-stepping) is achieved by a fourth-order Runge–Kutta algorithm. The noise in the initial conditions (27) is realized using MATLABs 'rand.m' function, which generates random numbers that are uniformly distributed in the interval [0, 1]. We impose zero-Dirichlet boundary conditions at the outer boundaries. Because Dirichlet boundary conditions are reflective rather than absorbing, special care is taken to assure that reflections from the numerical boundaries have no effect (see also Section 9.2). In particular, simulations showing multiple filamentation are verified by enlarging the computational domain, as well as by refining the grid.

In most simulations of Eq. (26) the symmetries in the x and y directions enable us to solve the equation on one quadrant of the plane. However, in the rotation simulation of Fig. 25, these symmetries cannot be exploited. The simulations in Section 6 are also carried on the whole (x, y) plane, since otherwise the noise would be symmetric in the x and y directions, in which case it would be less likely to lead to a complete break-up of cylindrical symmetry.

9.1. Physical or grid-induced splitting

As noted in Section 4, vectorial effects induce a preferred direction in the transverse (x, y) plane, which, in our model, is the x-axis direction. Therefore, in the case of cylindrically symmetric input beams, when vectorial effects
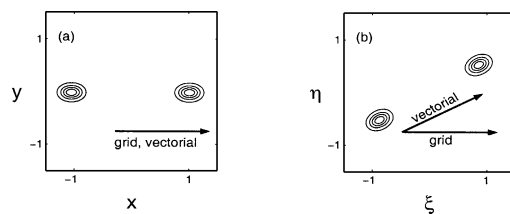

Fig. 25. Contour plots at $z = 0.32$ of the solution of (26) with the same parameters as in Fig. 20 and $N(0) = 5N_c$. (a) Computed in the (x, y) plane. (b) Computed in the $(\tilde{x}, \tilde{y})$ plane ($\theta_0 = 30°$). Arrows show preferred directions of the numerical grid and of the vectorial perturbation terms.

lead to breakup of the beam into two filaments, the two filaments can move away from each other either along the direction of initial polarization or perpendicular to it. Indeed, in our simulations the filaments move away in either of these directions. However, the Cartesian grid that we use in our simulations also has the preferred x and y directions. Therefore, we would like to make sure that the splitting in these simulations is due to vectorial effects, rather than to grid effects.

To do that, we solve Eq. (26) using the same parameters and input beam as in Fig. 8, but in the rotated coordinate system:

$$(\xi, \eta) = (x \cos \theta_0 - y \sin \theta_0, x \sin \theta_0 + y \cos \theta_0),$$

where θ_0 is the angle of rotation. Since in the rotated (ξ, η) system the preferred direction of vectorial effects forms an angle of θ_0 with $\hat{e}_\xi$, there is now a clear distinction between the preferred direction of vectorial effects and that of grid effects. We note that NLS and nonparaxial terms in Eq. (26) remain the same under rotations. The vectorial perturbation terms in Eq. (26) do change under rotations, according to:

$$A_{1,x} = A_{1,\xi} \cos \theta_0 + A_{1,\eta} \sin \theta_0, \qquad A_{1,xx} = A_{1,\xi\xi} \cos^2 \theta_0 + A_{1,\xi\eta} \sin(2\theta_0) + A_{1,\eta\eta} \sin^2 \theta_0.$$

In the simulation in Fig. 25 we take $\theta_0 = 30°$. We observe the same dynamics as when $\theta_0 = 0°$, except that the direction of beam-splitting and filament propagation in the (ξ, η) plane follows the preferred direction of the vectorial effects. Thus, this simulation shows that the multiple filamentation observed in our simulations is a feature of the PDE (26), rather than a numerical artifact.

9.2. Boundary-induced filaments

We now show that when the computational domain is not sufficiently large, reflections from the boundary can lead to what may appear as breakup of cylindrical symmetry and even as multiple filamentation. To see that, we carry three simulations of Eq. (36) with the same high-power input beam. The first simulation, which serves as a benchmark, is over a larger domain with Dirichlet boundary conditions. The other two simulations are over a smaller
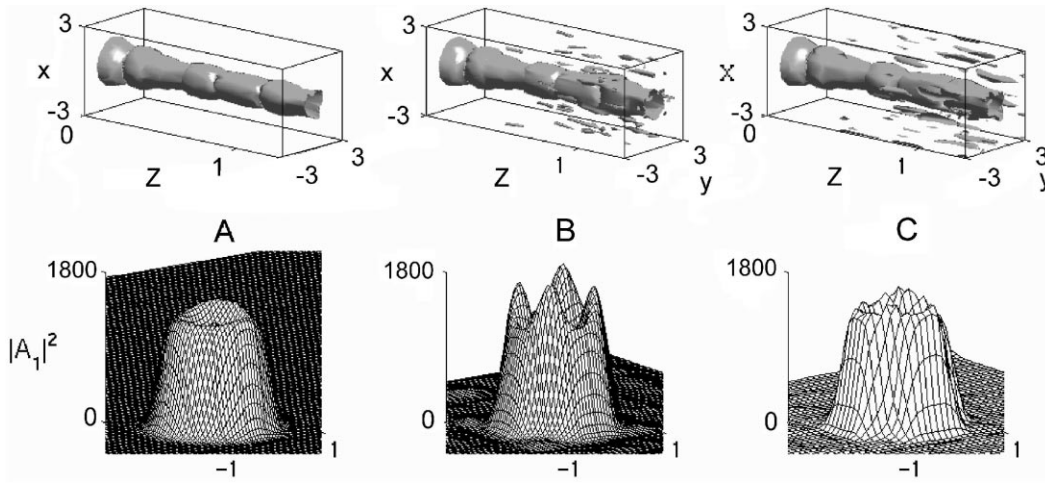
Fig. 26. Solution of Eq. (36) with $\epsilon = 0.01$ and with the input beam $A_1(x, y, z = 0) = 36 e^{-(x^2+y^2)\ln(2)}[1 + 0.02 \, \text{noise}(x, y)]$ (i.e., $N(0) \approx 253 N_c$). Computational domain and boundary conditions are (A) $(x, y) \in [-8, 8]^2$, Dirichlet boundary conditions. (B) $(x, y) \in [-3, 3]^2$, Dirichlet boundary conditions. (C) $(x, y) \in [-3, 3]^2$, periodic boundary conditions. Top: iso-surface $|A_1|^2 = 30$. Bottom: 3D plot at $z = 0.9$.

computational domain, on which we impose either Dirichlet or periodic boundary conditions. For consistency, we use *the same noise function realization* in the two simulations over the smaller domain and extend this noise function in the (x, y) plane with zero values for the simulation over the larger domain.

In the simulation over the larger domain we do not observe multiple filamentation for $0 \leq z \leq 0.9$ (Fig. 26A, top). In addition, at $z = 0.9$ the beam has an almost-symmetric ring structure (Fig. 26A, bottom). In contrast, we observe filament-type patterns in the iso-surfaces of the two simulations over the smaller domain (top of Fig. 26B and C). Moreover, in the simulation over the smaller domain with Dirichlet boundary conditions the ring at $z = 0.9$ is asymmetric (Fig. 26B, bottom). Thus, the filaments observed in the simulations over the smaller domain, as well as the breakup of symmetry of the ring, are a numerical artifact.

10. Final remark

In this study we derive a scalar PDE for self-focusing in the presence of vectorial and nonparaxial effects. When the input power $N(0)$ is only moderately above the critical power N_c, the propagation dynamics can by analyzed using modulation theory, and is thus fairly well understood. Unfortunately, there is no such theory for the high-power regime $N(0) \gg N_c$, at which multiple filamentation takes place. Therefore, at present, we can only rely on numerical simulations to explore vectorial (and random) effects in this regime. Several key-questions still await an answer, such as: (1) How does the threshold power for multiple filamentation depend on the model parameters? (2) How do the number and pattern of the filaments depend on the input power? (3) What is the effect, in any, of plasma generation and time dispersion on multiple filamentation of ultrashort pulses?

Perhaps the most important open question is whether vectorial effects or noise are the mechanism leading to multiple filamentation. We believe that the results of this study support the vectorial effects explanation, at least when the input power is only a few times N_c. A definite answer, however, would probably come from the experimental test suggested in Section 8.

Acknowledgements

Appendix A. Derivation of (19) and (20)

The input beam is linearly polarized in the x direction, i.e.,

$$A_2 = A_3 = 0 \quad \text{at} \ z = 0. \tag{A.1}$$

Therefore, to leading order, the beam remains linearly polarized over propagation distances of several diffraction lengths, i.e.,

$$A_1 = \mathrm{O}(1), \qquad A_2 = \mathrm{o}(1), \qquad A_3 = \mathrm{o}(1). \tag{A.2}$$

From Eq. (18) and (A.2), we have that

$$N_1 = \mathrm{O}(1), \tag{A.3}$$

$$N_2 = G_1(A_1) \cdot A_2 + G_2(A_1) \cdot A_2^* + o(1), \tag{A.4}$$

$$N_3 = G_3(A_1) \cdot A_3 + G_4(A_1) \cdot A_3^* + o(1), \tag{A.5}$$

where the functions $G_i\,(i = 1, 2, 3, 4)$ are O(1). Using Eqs. (A.2)–(A.5), we can rewrite Eq. (17) as

$$A_3 = \mathrm{i}f\nabla_\perp \cdot \vec{A} + f^2[-\tfrac{1}{2}A_{3,z} + \mathrm{i}G_3(A_1) \cdot A_3 + \mathrm{i}G_4(A_1) \cdot A_3^*] + \mathrm{O}(f^3).$$

From this equation and Eq. (A.2), we can conclude that

$$A_3 = \mathrm{i}f(A_{1,x} + A_{2,y}) + \mathrm{O}(f^3) = \mathrm{O}(f). \tag{A.6}$$

Using Eqs. (18) and (A.6), we can rewrite Eq. (A.4) as

$$N_2 = G_1(A_1) \cdot A_2 + G_2(A_1) \cdot A_2^* + \mathrm{O}(f^2). \tag{A.7}$$

The second component of the Helmholtz equation (16) reads

$$\mathrm{i}A_{2,z} + \Delta_\perp A_2 + N_2 + \tfrac{1}{4}f^2 A_{2,zz} = -f\,\partial_y(f\nabla_\perp \cdot \vec{N} + \mathrm{i}N_3 + \tfrac{1}{2}f^2 N_{3,z}). \tag{A.8}$$

In light of Eqs. (A.2)–(A.6), the right-hand side of Eq. (A.8) is $\mathrm{O}(f^2)$. Therefore, using Eq. (A.7) we can rewrite Eq. (A.8) as

$$\mathrm{i}A_{2,z} = -\Delta_\perp A_2 - G_1(A_1) \cdot A_2 + G_2(A_1) \cdot A_2^* + \mathrm{O}(f^2). \tag{A.9}$$

From (A.1) and (A.9) we obtain (19). The estimate (20) follows from (A.6) and (19).

Appendix B. Proof of Proposition 3.1

The first component of the Helmholtz equation (16) is

$$\mathrm{i}A_{1,z} + \Delta_\perp A_1 + N_1 + \tfrac{1}{4}f^2 A_{1,zz} + f\,\partial_x(f\nabla_\perp \cdot \vec{N} + \mathrm{i}N_3 + \tfrac{1}{2}f^2 N_{3,z}) = 0. \tag{B.1}$$

In light of Eqs. (A.5) and (A.6), we have that $N_3 = \mathrm{O}(f)$. Therefore, Eq. (B.1) can be rewritten as

$$\mathrm{i}A_{1,z} + \Delta_\perp A_1 + N_1 + \tfrac{1}{4}f^2 A_{1,zz} + f\,\partial_x(f\nabla_\perp \cdot \vec{N} + \mathrm{i}N_3) = \mathrm{O}(f^4). \tag{B.2}$$

In order to simplify the terms that depend on $\vec{N}$, we use the estimates (19) and (20) to obtain from Eq. (18) that

$$N_1 = |A_1|^2 A_1 + \frac{f^2}{1+\gamma}[|A_{1,x}|^2 A_1 - \gamma(A_{1,x})^2 A_1^*] + \mathrm{O}(f^4), \tag{B.3}$$

$$N_3 = \frac{\mathrm{i}f}{1+\gamma}(|A_1|^2 A_{1,x} - \gamma A_1^2 A_{1,x}^*) + \mathrm{O}(f^3),$$

$$\nabla_\perp \cdot \vec{N} = N_{1,x} + N_{2,y} = 2|A_1|^2 A_{1,x} + A_1^2 A_{1,x}^* + \mathrm{O}(f^2). \tag{B.3}$$

Substituting the estimates (B.3) in Eq. (B.2), we obtain the scalar equation

$$\mathrm{i}A_{1,z} + \Delta_\perp A_1 + |A_1|^2 A_1 + \frac{f^2}{1+\gamma}[|A_{1,x}|^2 A_1 - \gamma(A_{1,x})^2 A_1^*] + \frac{1}{4}f^2 A_{1,zz}$$

$$+ f^2 \partial_x\left[(2|A_1|^2 A_{1,x} + A_1^2 A_{1,x}^*) - \frac{1}{1+\gamma}(|A_1|^2 A_{1,x} - \gamma A_1^2 A_{1,x}^*)\right] = \mathrm{O}(f^4),$$

which can be simplified to give Eq. (21).

Appendix C. Derivation of (23)

Lemma C.1. *The components of the Lagrangian $\mathcal{L}_{\mathrm{VH}}$ (22) can be approximated with*

$$\mathcal{E}_{k,k}\mathcal{E}_{j,j}^* = \mathrm{O}(f^6), \tag{C.1}$$

$$\mathcal{E}_{j,k}\mathcal{E}_{j,k}^* = \frac{f^2 n_0}{4r_0^2 \bar{n}_2} \left\{ \left[\frac{1}{f^2}|A_1|^2 + \frac{1}{f^2}|A_2|^2 + |A_{1,x}|^2 \right] + \left[-\frac{\mathrm{i}}{2}(A_1^* A_{1,z} - A_1 A_{1,z}^*) + |A_{1,x}|^2 + |A_{1,y}|^2 \right] \right.$$

$$\left. + f^2 \left[\frac{1}{4}|A_{1,z}|^2 + |A_{1,xx}|^2 + |A_{1,xy}|^2 - \frac{\mathrm{i}}{2}(A_{1,xz}A_{1,x}^* - A_{1,xz}^* A_{1,x}) \right] \right\} + \mathrm{O}(f^6), \tag{C.2}$$

$$k_0^2 \mathcal{E}_k \mathcal{E}_k^* = \frac{f^2 n_0}{4r_0^2 \bar{n}_2} \left[\frac{1}{f^2}|A_1|^2 + \frac{1}{f^2}|A_2|^2 + |A_{1,x}|^2 \right] + \mathrm{O}(f^6) \tag{C.3}$$

and

$$\frac{2k_0^2 \bar{n}_2}{n_0(1+\gamma)}(\delta_i^l \delta_j^k + \gamma \delta_i^k \delta_j^l)\mathcal{E}_i \mathcal{E}_j^* \mathcal{E}_k \mathcal{E}_l^*$$

$$= \frac{f^2 n_0}{4r_0^2 \bar{n}_2}\frac{1}{2}|A_1|^4 + \frac{f^2 n_0}{4r_0^2 \bar{n}_2}\frac{f^2}{2(1+\gamma)}\{2|A_1|^2|A_{1,x}|^2 - \gamma[(A_{1,x})^2 A_1^{*2} + (A_{1,x}^*)^2 A_1^2]\} + \mathrm{O}(f^6). \tag{C.4}$$

Proof. Using the rescaling (15) and substituting the estimates (19) and (20) we have that

$$\mathcal{E}_{k,k}\mathcal{E}_{j,j}^* \stackrel{(15)}{=} \frac{f^2 n_0}{4r_0^2 \bar{n}_2}\left| A_{1,x} + \frac{\mathrm{i}}{f}A_3 + \mathrm{O}(f^2)\right|^2 \stackrel{(19),(20)}{=} \frac{f^2 n_0}{4r_0^2 \bar{n}_2}\cdot \mathrm{O}(f^4) = \mathrm{O}(f^6), \tag{C.5}$$

which proves (C.1). Similarly,

$$\mathcal{E}_{j,k}\mathcal{E}_{j,k}^* \stackrel{(15)}{=} \frac{f^2 n_0}{4\bar{n}_2}\left(\left|\frac{A_{1,x}}{r_0}\right|^2 + \left|\frac{A_{1,y}}{r_0}\right|^2 + \left|\frac{A_{1,z}}{2k_0 r_0^2} + \mathrm{i}k_0 A_1\right|^2 + \left|\frac{A_{2,x}}{r_0}\right|^2 + \left|\frac{A_{2,y}}{r_0}\right|^2 + \left|\frac{A_{2,z}}{2k_0 r_0^2} + \mathrm{i}k_0 A_2\right|^2 \right.$$

$$\left. + \left|\frac{A_{3,x}}{r_0}\right|^2 + \left|\frac{A_{3,y}}{r_0}\right|^2 + \left|\frac{A_{3,z}}{2k_0 r_0^2} + \mathrm{i}k_0 A_3\right|^2 \right)$$

$$\stackrel{(19),(20)}{=} \frac{f^2 r_0^4 n_0}{4\bar{n}_2}\left(|A_{1,x}|^2 + |A_{1,y}|^2 + \left|\frac{1}{2}fA_{1,z} + \frac{\mathrm{i}}{f}A_1\right|^2 + \left|\frac{\mathrm{i}}{f}A_2\right|^2 + |\mathrm{i}fA_{1,xx}|^2 + |\mathrm{i}fA_{1,xy}|^2 \right.$$

$$\left. + \left|\frac{1}{2}\mathrm{i}f^2 A_{1,xz} + \mathrm{i}A_{1,x}\right|^2 \right) + \mathrm{O}(f^6),$$

which gives (C.2). Relation (C.3) is straightforward. Finally,

$$\frac{2k_0^2\bar{n}_2}{n_0(1+\gamma)}(\delta_i^l\delta_j^k + \gamma\delta_i^k\delta_j^l)\mathcal{E}_i\mathcal{E}_j^*\mathcal{E}_k\mathcal{E}_l^* \stackrel{(15)}{=} \frac{2k_0^2\bar{n}_2}{n_0(1+\gamma)}\frac{f^4n_0^2}{16\bar{n}_2^2}(A_iA_i^*A_kA_k^* + \gamma A_iA_iA_k^*A_k^*)$$

$$= \frac{f^2n_0}{4r_0^2\bar{n}_2}\frac{f^2}{2(1+\gamma)}[(|A_1|^2 + |A_2|^2 + |A_3|^2)^2 + \gamma|A_1^2 + A_2^2 + A_3^2|^2] + O(f^4)$$

$$\stackrel{(19),(20)}{=} \frac{f^2n_0}{4r_0^2\bar{n}_2}\frac{f^2}{2(1+\gamma)}[(|A_1|^2 + f^2|A_{1,x}|^2)^2 + \gamma|A_1^2 - if^2A_{1,x}^2|^2] + O(f^4),$$

which gives (C.4). □

Substituting Eqs. (C.1)–(C.4) in (22) and dividing by $f^2n_0/4r_0^2\bar{n}_2$ gives (23).

Appendix D. Proof of Proposition 3.2

Eqs. (21) and (24) have the same O(1) and nonparaxial terms. Therefore, the difference between these equations comes only from the vectorial terms, and is given by

$$\text{Eq.(21)} - \text{Eq.(24)} = f^2\left\{-\frac{4+6\gamma}{1+\gamma}|A_{1,x}|^2A_1 - (A_{1,x})^2A_1^* - \frac{1+2\gamma}{1+\gamma}(|A_1|^2A_{1,xx} + A_1^2A_{1,xx}^*)\right.$$

$$+\frac{1}{1+\gamma}[2\gamma|A_{1,x}|^2A_1 - (1+\gamma)(A_{1,x})^2A_1^* - |A_1|^2A_{1,xx} + \gamma A_1^2A_{1,xx}^*]$$

$$\left.-\partial_{xx}(iA_{1,z} + \Delta_\perp A_1)\right\} + O(f^4). \tag{D.1}$$

We now prove that this difference is $O(f^4)$, rather than $O(f^2)$. To do that, we differentiate Eq. (24) twice with respect to x, to obtain

$$\partial_{xx}(iA_{1,z} + \Delta_\perp A_1 + |A_1|^2A_1) = O(f^2).$$

Therefore,

$$\partial_{xx}(iA_{1,z} + \Delta_\perp A_1) = -[4|A_{1,x}|^2A_1 + 2(A_{1,x})^2A_1^* + 2|A_1|^2A_{1,xx} + A_1^2A_{1,xx}^*] + O(f^2).$$

Substituting this equation in Eq. (D.1) gives that

$$\text{Eq.(21)} - \text{Eq.(24)} = f^2\left\{-\frac{4+6\gamma}{1+\gamma}|A_{1,x}|^2A_1 - (A_{1,x})^2A_1^* - \frac{1+2\gamma}{1+\gamma}(|A_1|^2A_{1,xx} + A_1^2A_{1,xx}^*)\right.$$

$$+\frac{1}{1+\gamma}[2\gamma|A_{1,x}|^2A_1 - (1+\gamma)(A_{1,x})^2A_1^* - |A_1|^2A_{1,xx} + \gamma A_1^2A_{1,xx}^*]$$

$$\left.+[4|A_{1,x}|^2A_1 + 2(A_{1,x})^2A_1^* + 2|A_1|^2A_{1,xx} + A_1^2A_{1,xx}^*]\right\} + O(f^4).$$

Technical calculations show that the $O(f^2)$ terms on the right-hand side cancel each other. Therefore, the difference between Eqs. (21) and (24) is only $O(f^4)$.

Appendix E. Proof of Eq. (25)

Let us denote

$$W := \Delta_\perp A_1 + |A_1|^2 A_1. \tag{E.1}$$

Using either of the scalar equations (24) or (21), we have that

$$A_{1,z} = iW + O(f^2). \tag{E.2}$$

Therefore, differentiating (E.2) with respect to z and using (E.1) and (E.2), we get that

$$A_{1,zz} \stackrel{(E.2)}{=} iW_z + O(f^2) \stackrel{(E.1)}{=} i\Delta_\perp A_{1,z} + 2i|A_1|^2 A_{1,z} + iA_1^2 A_{1,z}^* + O(f^2)$$

$$\stackrel{(E.2)}{=} -\Delta_\perp W - 2|A_1|^2 W + A_1^2 W^* + O(f^2). \tag{E.3}$$

Substituting (E.1) in the right-hand side of (E.3), we obtain

$$A_{1,zz} = -\Delta_\perp^2 A_1 - \Delta_\perp(|A_1|^2 A_1) - 2|A_1|^2 \Delta_\perp A_1 + A_1^2 \Delta_\perp A_1^* - |A_1|^4 A_1 + O(f^2). \tag{E.4}$$

Eq. (25) follows from Eq. (E.4) and the vectorial identity

$$\Delta_\perp(|A_1|^2 A_1) \equiv 2|A_1|^2 \Delta_\perp A_1 + 4(\nabla_\perp A_1) \cdot (\nabla_\perp A_1^*) A_1 + 2(\nabla_\perp A_1) \cdot (\nabla_\perp A_1) A_1^* + A_1^2 \Delta_\perp A_1^*.$$

Appendix F. Modulation theory for vectorial and nonparaxial effects

F.1. Modulation theory

In order to conform to the notations of [20], we denote $\psi = A_1$, $\epsilon = f^2$, and rewrite Eq. (21) as the perturbed NLS

$$i\psi_z + \Delta_\perp \psi + |\psi|^2 \psi + \epsilon F[\psi] = 0, \tag{F.1}$$

where $F[\psi] = P[\psi] + G[\psi] + H[\psi] + K[\psi]$ and

$$P[\psi] = \frac{1}{4}\psi_{zz}, \qquad G[\psi] = \frac{4 + 6\gamma}{1 + \gamma}|\psi_x|^2 \psi, \qquad H[\psi] = (\psi_x)^2 \psi^*,$$

$$K[\psi] = \frac{1 + 2\gamma}{1 + \gamma}(|\psi|^2 \psi_{xx} + \psi^2 \psi_{xx}^*). \tag{F.2}$$

Here $P[\psi]$ corresponds to nonparaxiality, and $G[\psi]$, $H[\psi]$, and $K[\psi]$ correspond to vectorial effects.

Modulation theory is based on the following assumptions:

- The focusing part of a filament is close to the asymptotic profile $\psi_R(r, z)$, which is given by

$$\psi_R(r, z) := \frac{1}{L(z)} R(\rho) e^{iS}, \tag{F.3}$$

where $R(\rho)$ is defined in Eq. (10),

$$\rho(r, z) := \frac{r}{L(z)}, \qquad S(r, z) := \zeta(z) + \frac{r^2 L_z(z)}{4L(z)}, \qquad \zeta_z(z) := \frac{1}{L^2(z)}. \tag{F.4}$$

- The filament's power is close to the critical power N_c.
- The perturbation terms are small, i.e., $|\epsilon F| \ll |\Delta_\perp \psi|$ and $|\epsilon F| \ll |\psi|^3$.

Under these assumptions, self-focusing dynamics of the perturbed NLS (F.1) is described, to leading order, by

$$L_{zz}(z) = -\frac{\beta}{L^3}, \qquad \beta_z(z) = \frac{\epsilon}{2M}(f_{1,z} - 4f_2), \tag{F.5}$$

where N_c and M are defined in Eqs. (11) and (30), respectively, and the auxiliary functions for $F[\psi]$ are given by

$$f_1(z) = \frac{L}{\pi} \mathrm{Re} \int F[\psi_R][R(\rho) + \rho R'(\rho)] \, \mathrm{e}^{-iS} \, \mathrm{d}x \, \mathrm{d}y, \qquad f_2(z) = \frac{1}{2\pi} \mathrm{Im} \int F[\psi_R]\psi_R^* \, \mathrm{d}x \, \mathrm{d}y. \tag{F.6}$$

Because Eq. (F.6) is linear in F, the reduced system (F.5) is additive in the perturbation terms. Therefore, in our case we get that

$$f_1 = p_1 + g_1 + h_1 + k_1, \qquad f_2 = p_2 + g_2 + h_2 + k_2, \tag{F.7}$$

where p_i $(i = 1, 2)$ are the auxiliary functions with $P[\psi_R]$ instead of $F[\psi_R]$ in Eqs. (F.6), and similarly for g_i, h_i, and k_i (see Appendix F.4).

Lemma F.1. *The auxiliary functions corresponding to P, G, H, and K in Eq.* (F.2) *satisfy:*

$$p_{1,z} \ll p_2, \quad p_2 \sim \frac{N_c}{4}\left(\frac{1}{L^2}\right)_z, \qquad g_2 \equiv 0, \qquad g_{1,z} \sim \frac{4+6\gamma}{3(1+\gamma)}N_c\left(\frac{1}{L^2}\right)_z, \qquad h_{1,z} \sim \frac{N_c}{3}\left(\frac{1}{L^2}\right)_z,$$

$$h_2 = \frac{N_c}{4}\left(\frac{1}{L^2}\right)_z, \qquad k_2 \equiv 0, \qquad k_{1,z} \sim \frac{2+4\gamma}{3(1+\gamma)}(3N_c - 2I_6)\left(\frac{1}{L^2}\right)_z,$$

where $I_6 \approx 6N_c$.

In order to prove Lemma F.1, we first make some preliminary calculations.

F.2. Preliminaries calculations

In the following calculations we switch back and forth between Cartesian and cylindrical coordinates, given by

$$(x, y) = (r\cos\theta, r\sin\theta) = \rho L(\cos\theta, \sin\theta).$$

We also denote $(\cdot)' := \frac{\mathrm{d}}{\mathrm{d}\rho}$.

The small parameter in modulation theory is $\beta(z)$. We can utilize this to simplify the expressions in Lemma F.3, by using the following relations:

Lemma F.2. *Let $|\beta| \ll 1$. Then, the following relations hold:*

$$[L^2 L_z^2] = [x^2 L_z^2] = O(\beta) \ll 1, \tag{F.8}$$

$$R_x^2 - (RS_x)^2 \sim R_x^2, \tag{F.9}$$

where $[\cdot]$ stands for the characteristic size.

Proof. These relations follow from $[x] = [L]$, $[S_x] = [LL_z]$, and $|\beta| = |L^3 L_{zz}| \ll 1$. $\qquad\square$

Lemma F.3. Let ψ_R be given by (F.3) and (F.4). Then:

$$|\psi_{R,x}|^2 \sim L^{-4} R'^2 \cos^2\theta, \tag{F.10}$$

$$\text{Im}[(\psi_{R,x})^2 \, e^{-2iS}] = L^{-2} (R^2)_x S_x, \tag{F.11}$$

$$\text{Re}[(\psi_{R,x})^2 \, e^{-2iS}] = L^{-4} R'^2 \cos^2\theta, \tag{F.12}$$

$$\text{Re}(\psi_R^* \psi_{R,xx}) \sim L^{-4} \left(RR'' \cos^2\theta + \frac{1}{\rho} RR' \sin^2\theta \right). \tag{F.13}$$

Proof. From (F.3) and (F.4) we obtain that

$$S_x = \frac{xL_z}{2L}, \qquad R_x = \frac{R' \cos\theta}{L}, \qquad R_{xx} = \frac{1}{L^2} \left(R'' \cos^2\theta + \frac{1}{\rho} R' \sin^2\theta \right). \tag{F.14}$$

Using Eqs. (F.3) and (F.4) we get that

$$\psi_{R,x} = L^{-1}(R_x + iRS_x) \, e^{iS}, \tag{F.15}$$

from which we obtain

$$|\psi_{R,x}|^2 \overset{\text{(F.15)}}{=} L^{-2}(R_x^2 + R^2 S_x^2) \overset{\text{(F.14)}}{=} L^{-4} \cos^2\theta (R'^2 + \tfrac{1}{4} R^2 \rho^2 L^2 L_z^2). \tag{F.16}$$

This expression can be further simplified using (F.8), because

$$R'^2 + \tfrac{1}{4} \rho^2 R^2 L^2 L_z^2 = R'^2 + O(L^2 L_z^2) \sim R'^2.$$

Substituting this approximation in (F.16) leads to (F.10). In addition, from (F.15) we have that

$$(\psi_{R,x})^2 = L^{-2} \, e^{2iS}[R_x^2 - (RS_x)^2 + i(R^2)_x S_x], \tag{F.17}$$

from which (F.11) follows. From (F.17) we also have that

$$\text{Re}[(\psi_{R,x})^2 \, e^{-2iS}] = L^{-2}[R_x^2 - (RS_x)^2] \overset{\text{(F.9)}}{\sim} L^{-2} R_x^2 \overset{\text{(F.14)}}{=} L^{-4} R'^2 \cos^2\theta,$$

which proves (F.12). Finally, we have that

$$\psi_{R,xx} \overset{\text{(F.15)}}{=} L^{-1} \, e^{iS}[(R_{xx} - RS_x^2) + i(2R_x S_x + RS_{xx})].$$

From this relation we get that

$$\text{Re}(\psi_R^* \psi_{R,xx}) \overset{\text{(F.3),(F.4)}}{=} \frac{R}{L^2}(R_{xx} - RS_x^2)$$

$$\overset{\text{(F.14)}}{=} \frac{R}{L^4} \left[\left(R'' \cos^2\theta + \frac{1}{\rho} R' \sin^2\theta \right) - \frac{1}{4} x^2 RL_z^2 \right] \overset{\text{(F.8)}}{\sim} \frac{R}{L^4} \left(R'' \cos^2\theta + \frac{1}{\rho} R' \sin^2\theta \right),$$

which proves (F.13). □

F.3. Integral relations

In this section we obtain relations (F.18), (F.20), (F.21) and (F.26), in order to reduce the number of constants that appear in the reduced system (29).

The following relation is well known

$$\int R^4 \rho \, d\rho = 2N_c. \tag{F.18}$$

We now prove some additional relations.

Lemma F.4. *Let $R(\rho)$ be defined by Eq. (10) and let*

$$I_1 := 3 \int R^2 R'^2 \rho \, d\rho, \qquad I_2 := 3 \int \rho R R'^3 \rho \, d\rho, \qquad I_3 := 3 \int \rho R^2 R' R'' \rho \, d\rho,$$

$$I_4 := 3 \int R^3 R'' \rho \, d\rho, \qquad I_6 := \int R^6 \rho \, d\rho. \tag{F.19}$$

Then the following relations hold:

$$I_1 + I_2 = N_c, \tag{F.20}$$

$$I_1 + I_3 + I_4 - \tfrac{3}{4} R^4(0) = 3N_c - 2I_6. \tag{F.21}$$

Proof. The proof will follow from the four linear equations (F.22)–(F.25) with $I_1, I_2, I_3, I_4, I_6, R(0)$, and N_c, which we now derive. Multiplying Eq. (10) by $(3\rho^2 R^2 R' \, d\rho)$ and integrating, we get that

$$\int (3\rho^2 R^2 R' R'' + 3\rho R^2 R'^2 + 3\rho^2 R^5 R' - 3\rho^2 R^3 R') \, d\rho = 0.$$

Using (F.19) we arrive at

$$I_3 + I_1 + \int \left[\frac{1}{2}\rho^2 (R^6)' - \frac{3}{4}\rho^2 (R^4)' \right] d\rho \overset{\text{IBP}}{=} I_3 + I_1 - \int \left(\rho R^6 - \frac{3}{2}\rho R^4 \right) d\rho = 0,$$

where "IBP" stands for integration-by-parts. Using (F.18), we obtain that

$$I_1 + I_3 = I_6 - 3N_c. \tag{F.22}$$

Multiplying (10) by $(R^3 \rho \, d\rho)$ and integrating we obtain

$$\int (\rho R^3 R'' + R^3 R' + \rho R^6 - \rho R^4) \, d\rho = 0.$$

Using (F.18) we obtain the second relation

$$\frac{1}{3} I_4 + \int_0^\infty \frac{1}{4} (R^4)' \, d\rho + I_6 - 2N_c = \frac{1}{3} I_4 - \frac{1}{4} R^4(0) + I_6 - 2N_c = 0. \tag{F.23}$$

From the definition of I_1 we have that

$$I_1 := 3 \int R^2 R' R' \rho \, d\rho \overset{\text{IBP}}{=} -3 \int (\rho R^2 R')' R \, d\rho \overset{(F.19)}{=} -\frac{3}{4} \int_0^\infty (R^4)' \, d\rho - 2I_1 - I_4 = \frac{3}{4} R^4(0) - 2I_1 - I_4,$$

which leads to the third relation

$$3I_1 + I_4 = \tfrac{3}{4} R^4(0). \tag{F.24}$$

Integration of the differential identity

$$\frac{3}{2}\frac{d}{d\rho}(\rho RR')^2 \equiv 3\rho R^2 R'^2 + 3\rho^2 RR'^3 + 3\rho^2 R^2 R' R'',$$

leads to the fourth relation

$$I_1 + I_2 + I_3 = 0. \tag{F.25}$$

Solving the linear system (F.22)–(F.25) we obtain

$$I_1 = I_6 - 2N_c, \qquad I_2 = 3N_c - I_6, \qquad I_3 = -N_c, \qquad I_4 = 6N_c - 3I_6 + \tfrac{3}{4}R^4(0),$$

from which (F.20) and (F.21) follow.   □

Finally, our numerical calculations show that $I_6 \approx 6.07N_c$. Therefore, we can use the approximation

$$I_6 \approx 6N_c, \tag{F.26}$$

which has about 1% accuracy.

F.4. Proof of Lemma F.1

The first perturbation term in Eq. (F.2) is the nonparaxial term $P[\psi]$. In [19] it was shown that

$$p_{1,z} \ll p_2 := \frac{1}{2\pi}\mathrm{Im}\int \frac{1}{4}\psi_{R,zz}\psi_R^*\,dx\,dy \sim \frac{N_c}{4}\left(\frac{1}{L^2}\right)_z. \tag{F.27}$$

Therefore, to leading order, p_1 can be neglected in the reduced system.

According to Eq. (F.6), the second auxiliary function corresponding to $G[\psi]$ is

$$g_2 := \frac{1}{2\pi}\frac{4+6\gamma}{1+\gamma}\int \mathrm{Im}(|\psi_{R,x}|^2|\psi_R^*|^2)\,dx\,dy = 0.$$

Calculating g_1 gives that

$$\begin{aligned}
g_1 &:= \frac{4+6\gamma}{1+\gamma}\frac{L}{\pi}\mathrm{Re}\int |\psi_{R,x}|^2\psi_R(R+\rho R')\,e^{-iS}\,dx\,dy \\
&\stackrel{\text{(F.3)}}{=} \frac{4+6\gamma}{1+\gamma}\pi\int |\psi_{R,x}|^2 R(R+\rho R')\,dx\,dy \\
&\stackrel{\text{(F.10)}}{\sim} \frac{4+6\gamma}{1+\gamma}\frac{1}{\pi L^4}\int R'^2\cos^2\theta(R^2+\rho RR')\,dx\,dy \\
&= \frac{4+6\gamma}{1+\gamma}\frac{1}{\pi L^2}\int_0^{2\pi}\cos^2\theta\,d\theta\int(R^2 R'^2+\rho RR'^3)\rho\,d\rho \\
&\stackrel{\text{(F.19)}}{=} \frac{4+6\gamma}{1+\gamma}\frac{1}{3L^2}(I_1+I_2)\stackrel{\text{(F.20)}}{=}\frac{4+6\gamma}{3(1+\gamma)}\frac{N_c}{L^2}.
\end{aligned} \tag{F.28}$$

For $H[\psi]$ we have that

$$\begin{aligned}
h_1 &:= \frac{L}{\pi}\mathrm{Re}\int (\psi_{R,x})^2\psi_R^*(R+\rho R')\,e^{-iS}\,dx\,dy \stackrel{\text{(F.3)}}{=}\frac{1}{\pi}\int \mathrm{Re}[(\psi_{R,x})^2]R(R+\rho R')\,dx\,dy \\
&\stackrel{\text{(F.12)}}{=} \frac{1}{\pi L^2}\int RR'^2(R+\rho R')\cos^2\theta\rho\,d\rho\,d\theta \stackrel{\text{(F.19)}}{=}\frac{1}{3L^2}(I_1+I_2)\stackrel{\text{(F.20)}}{=}\frac{N_c}{3L^2},
\end{aligned} \tag{F.29}$$

and

$$
\begin{aligned}
h_2 &:= \frac{1}{2\pi}\mathrm{Im}\int (\psi_{R,x})^2(\psi_R^*)^2 \, \mathrm{d}x\,\mathrm{d}y \overset{(F.3)}{=} \frac{1}{2\pi L^2}\int R^2\mathrm{Im}[(\psi_{R,x})^2\,\mathrm{e}^{-2\mathrm{i}S}]\,\mathrm{d}x\,\mathrm{d}y \\
&\overset{(F.11)}{=} \frac{1}{2\pi L^4}\int R^2(R^2)_x S_x \, \mathrm{d}x\,\mathrm{d}y = \frac{1}{4\pi L^4}\int (R^4)_x S_x \, \mathrm{d}x\,\mathrm{d}y \overset{\mathrm{IBP}}{=} -\frac{1}{4\pi L^4}\int R^4 S_{xx}\,\mathrm{d}x\,\mathrm{d}y \\
&\overset{(F.14)}{=} -\frac{L_z}{8\pi L^5}\int R^4 \, \mathrm{d}x\,\mathrm{d}y = -\frac{L_z}{8L^3}\int R^4\rho\,\mathrm{d}\rho \overset{(F.18)}{=} \frac{N_\mathrm{c}}{4}\left(\frac{1}{L^2}\right)_z .
\end{aligned}
\tag{F.30}
$$

For $K[\psi]$ we have that

$$
K[\psi_R]\psi_R^* = \frac{1+2\gamma}{1+\gamma}(|\psi_R|^2\psi_{R,xx} + \psi_R^2\psi_{R,xx}^*)\psi_R^* \overset{(F.3)}{=} \frac{2+4\gamma}{1+\gamma}\frac{R^2}{L^2}\mathrm{Re}(\psi_R^*\psi_{R,xx}).
\tag{F.31}
$$

In light of (F.31), the integrand in k_2 (F.6) is real valued. Therefore, $k_2 = 0$. Calculating k_1 gives that

$$
\begin{aligned}
k_1 &:= \frac{L}{\pi}\mathrm{Re}\int K[\psi_R](R+\rho R')\,\mathrm{e}^{-\mathrm{i}S}\,\mathrm{d}x\,\mathrm{d}y \overset{(F.3)}{=} \frac{L}{\pi}\int \mathrm{Re}\left(K[\psi_R]\psi_R^*\frac{L}{R}\right)(R+\rho R')\,\mathrm{d}x\,\mathrm{d}y \\
&\overset{(F.31)}{=} \frac{1+2\gamma}{1+\gamma}\frac{2}{\pi}\int \mathrm{Re}(\psi_R^*\psi_{R,xx})(R^2+\rho RR')\rho\,\mathrm{d}\rho \\
&\overset{(F.13)}{\sim} \frac{1+2\gamma}{1+\gamma}\frac{2}{\pi L^4}\int \left(RR''\cos^2\theta + \frac{1}{\rho}RR'\sin^2\theta\right)(R^2+\rho RR')\rho\,\mathrm{d}\rho \\
&\overset{(F.19)}{=} \frac{1+2\gamma}{1+\gamma}\frac{2}{3L^2}\left[I_4 + I_3 - \frac{3}{4}R^4(0) + I_1\right] \overset{(F.21)}{=} \frac{2+4\gamma}{3(1+\gamma)}(3N_\mathrm{c} - 2I_6)\frac{1}{L^2}.
\end{aligned}
\tag{F.32}
$$

Combining (F.27)–(F.30) and (F.32) proves Lemma F.1.

F.5. Proof of Proposition 5.1

To obtain Eqs. (29), we substitute the auxiliary functions of Lemma F.1 in Eq. (F.5), use Eq. (F.7), and use $\epsilon = f^2$. Doing that, to leading order we obtain

$$
\begin{aligned}
\beta_z &= \frac{f^2}{2M}(-4p_2 + g_{1,z} + h_{1,z} - 4h_2 + k_{1,z}) = \underbrace{-\frac{f^2 N_\mathrm{c}}{2M}\left(\frac{1}{L^2}\right)_z}_{\text{nonparaxial}} \\
&\quad + \underbrace{\frac{f^2}{2M}\left[\frac{4+6\gamma}{3(1+\gamma)}N_\mathrm{c} + \frac{1}{3}N_\mathrm{c} - N_\mathrm{c} + \frac{2+4\gamma}{3(1+\gamma)}(3N_\mathrm{c} - 2I_6)\right]\left(\frac{1}{L^2}\right)_z}_{\text{vectorial}},
\end{aligned}
$$

from which we obtain the second equation in (29) with $C_{\mathrm{np}} = 1$ and

$$
C_{\mathrm{vec}}(\gamma) = \frac{4}{3}\cdot\frac{(I_6/N_\mathrm{c} - 2) + (2I_6/N_\mathrm{c} - 4)\gamma}{1+\gamma} \overset{(F.26)}{\approx} \frac{16}{3}\left(1 + \frac{\gamma}{1+\gamma}\right).
$$

References

[1] S.C. Abbi, H. Mahr, Correlation of filaments in nitrobenzene with laser spikes, Phys. Rev. Lett. 26 (11) (1971) 604–606.
[2] J. Atai, Y. Chen, J.M. Soto-Crespo, Stability of three-dimensional self-trapped beams with a dark spot surrounded by bright rings of varying intensity, Phys. Rev. A 49 (1994) 3170–3173.

[3] T. Bergqvist, B. Kleman, P. Wahren, Breakdown phenomena in CS_2 caused by Nd-laser radiation, Ark. Fys. 34 (1967) 81–95.

[4] V.I. Bespalov, V.I. Talanov, Filamentary structure of light beams in nonlinear media, Zh. Eksper. Teor. Fiz. — Pis'ma Redakt. (USSR JETP) 3 (1966) 471–476 [Trans. in JETP Lett. 3 (1966) 307–310].

[5] J.E. Bjorkholm, A. Ashkin, Cw self-focusing and self-trapping of light in sodium vapor, Phys. Rev. Lett. 32 (1974) 129–132.

[6] R.W. Boyd, Nonlinear Optics, Academic Press, Boston, 1992.

[7] A. Braun, G. Korn, X. Liu, D. Du, J. Squier, G. Mourou, Self-channeling of high-peak-power femtosecond laser pulses in air, Opt. Lett. 20 (1995) 73–75.

[8] R.G. Brewer, J.R. Lifsitz, Narrow optical waveguides and instabilities induced in liquids, Phys. Lett. 23 (1966) 79–81.

[9] A. Brodeur, F.A. Ilkov, S.L. Chin, Beam filamentation and the white light continuum divergence, Opt. Commun. 129 (1996) 193–198.

[10] A. Brodeur, F.A. Ilkov, S.L. Chin, O.G. Kosareva, V.P. Kandidov, Moving focus in the propagation of ultrashort laser pulses in air, Opt. Lett. 22 (1997) 304–306.

[11] A.V. Butenin, V.V. Korobkin, A.A. Malyutin, M.Ya. Shchelv, Investigation of the kinetics of self-focusing in liquids, Zh. Eksper. Teor. Fiz. — Pis'ma Redakt. (USSR JETP) 6 (1967) 687–690 [Trans. in JETP Lett. 6 (1967) 173–176].

[12] A.J. Campillo, S.L. Shapiro, B.R. Suydam, Periodic breakup of optical beams due to self-focusing, Appl. Phys. Lett. 23 (1973) 628–630.

[13] S. Chi, Q. Guo, Vector theory of self-focusing of an optical beam in Kerr media, Opt. Lett. 20 (15) (1995) 1560–1598.

[14] R.Y. Chiao, M.A. Johnson, S. Krinsky, C.H. Townes, E. Garmire, 6A1 — a new class of trapped light filaments, IEEE J. Quant. Electron. QE- 2 (9) (1966) 467–469.

[15] Yu.S. Chilingarian, Self-focusing of inhomogeneous laser beams and its effect on stimulated scattering, Zh. Eksper. Teor. Fiz. — Pis'ma Redakt. (USSR JETP) 55 (5) (1968) 832–835 [Trans. in Sov. Phys. JETP 28 (1968) 832–835].

[16] B. Crosignani, P.D. Porto, A. Yariv, Nonparaxial equation for linear and nonlinear optical propagation, Opt. Lett. 22 (1997) 778–780 [Errata 22, 1820].

[17] R. de la Fuente, O. Varela, H. Michinel, Fourier analysis of non-paraxial self-focusing, Opt. Commun. 173 (2000) 403–411.

[18] M.D. Feit, J.A. Fleck, Beam nonparaxiality, filament formation, and beam breakup in the self-focusing of optical beams, J. Opt. Soc. Am. B 5 (1988) 633–640.

[19] G. Fibich, Small beam nonparaxiality arrests self-focusing of optical beams, Phys. Rev. Lett. 76 (1996) 4356–4359.

[20] G. Fibich, G.C. Papanicolaou, Self-focusing in the perturbed and unperturbed nonlinear Schrödinger equation in critical dimension, SIAM J. Appl. Math. 60 (1999) 183–240.

[21] G. Fibich, G.C. Papanicolaou, A modulation method for self-focusing in the perturbed critical nonlinear Schrödinger equation, Phys. Lett. A 239 (1998) 167–173.

[22] G. Fibich, S. Tsynkov, High-order two-way artificial boundary conditions for nonlinear wave propagation with backscattering. JCP, in press.

[23] S. Gatz, J. Hermann, Propagation of optical beams and the properties of two-dimensional spatial solitons in media with a local saturable nonlinear refractive index, J. Opt. Soc. Am. B 14 (1997) 1795–1805.

[24] Q. Guo, Private communication.

[25] C.S. Milsted Jr., C.D. Cantrell, Vector effects in self-focusing, Phys. Rev. A 53 (1996) 3536–3542.

[26] P.L. Kelley, Self-focusing of optical beams, Phys. Rev. Lett. 15 (26) (1965) 1005–1008.

[27] K. Konno, H. Suzuki, Self-focusing of a laser beam in nonlinear media, Phys. Scripta 20 (1979) 382–386.

[28] V.V. Korobkin, R.V. Serov, Investigation of self-focusing of neodymium-laser radiation, Zh. Eksper. Teor. Fiz. — Pis'ma Redakt. (USSR JETP) 6 (1967) 642–644 [Trans. in JETP Lett. 6 (1967) 135–137].

[29] M. Lax, W.H. Louisell, W.B. McKnight, From Maxwell to paraxial wave optics, Phys. Rev. A 11 (4) (1975) 1365–1370.

[30] G.J. Lord, Small-scale filaments in liquids and tracks of moving foci, Phys. Rev. Lett. 22 (1969) 994–997.

[31] P.D. Maker, R.W. Terhune, Study of optical effects due to an induced polarization third order in the electric field strength, Phys. Rev. 137 (1965) A801–A819.

[32] P.D. Maker, R.W. Terhune, C.M. Savage, Intensity-dependent changes in the refractive index of liquids, Phys. Rev. Lett. 12 (1964) 507–509.

[33] A.V. Mamaev, M. Saffman, D.Z. Anderson, A.A. Zozulya, Propagation of light beams in anisotropic nonlinear media: from symmetry breaking to spatial turbulence, Phys. Rev. A 54 (1996) 870–879.

[34] J.H. Marburger, E.L. Dawes, Dynamical formation of small-scale filaments, Phys. Rev. Lett. 21 (1968) 556–558.

[35] M. Mlejnek, M. Kolesik, J.V. Moloney, E.M. Wright, Optically turbulent femtosecond light guide in air, Phys. Rev. Lett. 83 (1999) 2938–2941.

[36] A.V. Nowak, D.O. Ham, Self-focusing of 10 μm laser pulses in SF_6, Opt. Lett. 6 (1981) 185–187.

[37] N.F. Pilipetskii, A.R. Rustamov, Observation of self-focusing of light in liquids, Zh. Eksper. Teor. Fiz. — Pis'ma Redakt. (USSR JETP) 2 (1965) 88–89 [Trans. in JETP Lett. 2 (1965) 55–56].

[38] J. Schwartz, P. Rambo, J.C. Diels, M. Kolesik, E.M. Wright, J.V. Moloney, Ultraviolet filamentation in air, Opt. Commun. 180 (2000) 383–390.

[39] J.M. Soto-Crespo, E.M. Wright, N.N. Akhmediev, Recurrence and azimuthal-symmetry breaking of a cylindrical Gaussian beam in a saturable self-focusing medium, Phys. Rev. A 45 (1992) 3168–3174.

[40] C. Sulem, P.L. Sulem, The Nonlinear Schrödinger Equation, Springer, New York, 1999.

[41] F. Vidal, T.W. Johnston, Electromagnetic beam breakup — multiple filaments, single beam equilibria and radiation, Phys. Rev. Lett. 77 (1996) 1282–1285.

[42] M.I. Weinstein, Nonlinear Schrödinger equations and sharp interpolation estimates, Commun. Math. Phys. 87 (1983) 567–576.